Available online at www.sciencedirect.com
ScienceDirect
Icarus 193 (2008) 182–212
ICARUS
www.elsevier.com/locate/icarus

A close look at Saturn's rings with Cassini VIMS

Philip D. Nicholson [a,*], Matthew M. Hedman [a], Roger N. Clark [b], Mark R. Showalter [c], Dale P. Cruikshank [d], Jeffrey N. Cuzzi [d], Gianrico Filacchione [e], Fabrizio Capaccioni [e], Priscilla Cerroni [e], Gary B. Hansen [f], Bruno Sicardy [g], Pierre Drossart [g], Robert H. Brown [h], Bonnie J. Buratti [i], Kevin H. Baines [i], Angioletta Coradini [j]

[a] *Department of Astronomy, Cornell University, Ithaca, NY 14853, USA*
[b] *USGS, Mail Stop 964, PO Box 25046, Federal Center, Denver, CO 80225, USA*
[c] *SETI Institute, 515 North Whisman Road, Mountain View, CA 94043, USA*
[d] *NASA Ames Research Center, Moffett Field, CA 94305, USA*
[e] *Istituto de Astrofisica Spaziale e Fisica Cosmica, Via del Fosso del Cavaliere 100, 00133 Rome, Italy*
[f] *Department of Earth & Space Sciences, Box 351310, University of Washington, Seattle, WA 98195, USA*
[g] *Observatoire de Paris, 5 Place Jules Janssen, F-92195, Meudon cedex, France*
[h] *Lunar & Planetary Laboratory, University of Arizona, Tucson, AZ 85721, USA*
[i] *Jet Propulsion Laboratory, 4800 Oak Grove Drive, Pasadena, CA 91109, USA*
[j] *Istituto de Astrofisica de Fisica dello Spazio Interplanetario, Via del Fosso del Cavaliere 100, 00133 Rome, Italy*

Received 30 November 2006; revised 7 August 2007

Available online 5 October 2007

Abstract

Soon after the Cassini–Huygens spacecraft entered orbit about Saturn on 1 July 2004, its Visual and Infrared Mapping Spectrometer obtained two continuous spectral scans across the rings, covering the wavelength range 0.35–5.1 μm, at a spatial resolution of 15–25 km. The first scan covers the outer C and inner B rings, while the second covers the Cassini Division and the entire A ring. Comparisons of the VIMS radial reflectance profile at 1.08 μm with similar profiles at a wavelength of 0.45 μm assembled from Voyager images show very little change in ring structure over the intervening 24 years, with the exception of a few features already known to be noncircular. A model for single-scattering by a classical, many-particle-thick slab of material with normal optical depths derived from the Voyager photopolarimeter stellar occultation is found to provide an excellent fit to the observed VIMS reflectance profiles for the C ring and Cassini Division, and an acceptable fit for the inner B ring. The A ring deviates significantly from such a model, consistent with previous suggestions that this region may be closer to a monolayer. An additional complication here is the azimuthally-variable average optical depth associated with "self-gravity wakes" in this region and the fact that much of the A ring may be a mixture of almost opaque wakes and relatively transparent interwake zones. Consistently with previous studies, we find that the near-infrared spectra of all main ring regions are dominated by water ice, with a typical regolith grain radius of 5–20 μm, while the steep decrease in visual reflectance shortward of 0.6 μm is suggestive of an organic contaminant, perhaps tholin-like. Although no materials other than H_2O ice have been identified with any certainty in the VIMS spectra of the rings, significant radial variations are seen in the strength of the water–ice absorption bands. Across the boundary between the C and B rings, over a radial range of ~7000 km, the near-IR band depths strengthen considerably. A very similar pattern is seen across the outer half of the Cassini Division and into the inner A ring, accompanied by a steepening of the red slope in the visible spectrum shortward of 0.55 μm. We attribute these trends—as well as smaller-scale variations associated with strong density waves in the A ring—to differing grain sizes in the tholin-contaminated icy regolith that covers the surfaces of the decimeter-to-meter sized ring particles. On the largest scale, the spectral variations seen by VIMS suggest that the rings may be divided into two larger 'ring complexes,' with similar internal variations in structure, optical depth, particle size, regolith texture and composition. The inner complex comprises the C and B rings, while the outer comprises the Cassini Division and A ring.
© 2007 Elsevier Inc. All rights reserved.

* Corresponding author.
E-mail address: nicholso@astro.cornell.edu (P.D. Nicholson).

0019-1035/$ – see front matter © 2007 Elsevier Inc. All rights reserved.
doi:10.1016/j.icarus.2007.08.036

Keywords: Planetary rings; Saturn, rings; Infrared observations

1. Introduction

Saturn's rings provided one of the earliest successful applications of ground-based near-infrared spectroscopy with the discovery that the rings are composed of—or covered by—H_2O in the form of ice or frost (Kuiper, 1952, 1957; Moroz, 1967). In his chapter in 'The Atmospheres of the Earth and Planets' (second ed., 1957, pp. 364–365) Kuiper writes, "Of special interest is the question of the composition of the rings of Saturn. The writer had expected to find a neutral reflection spectrum such as that from rock, although the high visual albedo of the rings might have led one to suspect otherwise. The reflection spectrum appears to be very similar to that of the polar cap of Mars; the water-cell equivalent of about 2/3 mm. It is provisionally concluded that the rings are covered by frost, if not composed of ice." Although this conclusion was initially based simply on the depression of the near-infrared spectrum in the region beyond 1.5 μm, by 1970 the two strong water ice bands centered at 1.5 and 2.0 μm had been spectrally resolved and the identification clinched (Kuiper et al., 1970; Pilcher et al., 1970; Lebofsky et al., 1970).

While the work cited above was based on simple comparisons of 1–3 μm telescopic spectra with laboratory spectra of H_2O ice at various temperatures, Pollack et al. (1973) published the first models of the reflectance spectra of the rings, using scattering theory and the optical properties of water ice, concluding that typical particle radii were in the 25–125 μm range.

The 1970s and 1980s also saw the first microwave observations of the rings, motivated by their surprisingly strong detection in radar observations at 13 cm wavelength (Goldstein and Morris, 1973; Goldstein et al., 1977; Ostro et al., 1980). Because the rings had never been convincingly detected in microwave emission, the large radar return quickly led to the conclusion that the ring particles had to be on the order of the wavelength in size (Pollack et al., 1973; Pettengill and Hagfors, 1974; Pollack, 1975). Subsequent radiometric observations of finite, but very low, ring brightness temperatures (see Esposito et al., 1984 for a review) could be reconciled with the strong radar returns only if the ring particles were not only wavelength-size, with power-law size distributions, but also made of nearly pure water ice (Cuzzi and Pollack, 1978; Cuzzi et al., 1980; Epstein et al., 1984). Grossman (1990) estimated the fraction of silicate material within the rings to be 1% or less, on the assumption that it is uniformly distributed within the ring particles.

These conclusions were reinforced by the Voyager radio occultation experiment (Tyler et al., 1983) from which Marouf et al. (1983) and Zebker et al. (1985) derived particle size distributions for optically thin parts of the A and C rings and the Cassini Division which spanned the range 1 cm to 10 m. A power-law size distribution with an incremental index, $q \simeq 3$ and a lower cutoff of 1 cm was found to fit these observations, with relatively few particles exceeding a radius of ∼5 m. Observations of Voyager and ground-based stellar occultations (Showalter and Nicholson, 1990; French and Nicholson, 2000) have confirmed that the optical cross-section of the rings is also dominated by particles in the 1 cm to 10 m size range, while analysis of Voyager photometry for the A ring showed a negligible contribution by micron-sized 'dust' to scattered light at optical wavelengths, even at high phase angles (Dones et al., 1993).

Clark and McCord (1980) published new 1.0–2.5 μm spectra of the rings and summarized the existing observational data, including ultraviolet and visual spectra by Lebofsky and Fegley (1976) as well as observations by Puetter and Russell (1977) which extended the spectral coverage of ground-based infrared data to 4.1 μm. This revealed the strong fundamental absorption band of water ice centered at ∼2.9 μm, as well as the Fresnel reflectance peak at 3.1 μm and a broad peak in reflectance at 3.6 μm. Model fits to these data by Clark et al. (1986), using the methods of Clark and Roush (1984), showed that the 3.6 μm peak—which is defined by strong ice absorptions at 2.9 and ∼4.5 μm—is quite sensitive to grain size. They obtained an average grain size of 30 μm, but this was now understood as referring to the frosty regolith which must cover the individual decimeter-sized ring particles. A similar conclusion was reached by Doyle et al. (1989), based on both the 3.1 and 3.6 μm peaks, who estimated that $r_g = 20$ μm.

However, pure water ice should have a flat visible spectrum down to ∼0.3 μm, whereas the average ring spectrum exhibits a strong red slope shortward of 0.6 μm [see the summary by Esposito et al. (1984) or Karkoschka (1994) for a more recent HST spectrum]. Analyses of the ultraviolet–visual color of the A and B rings have led several investigators, including Lebofsky et al. (1970), Irvine and Lane (1973) and Clark (1980), to conclude that the rings must also contain a well-mixed, non-icy component in order to account for their pronounced reddish color. Initial hypotheses centered on frosts containing either irradiated NH_3 or H_2S hydrates (Lebofsky and Fegley, 1976), sulfur allotropes (Gradie et al., 1980) or some form of Fe^{3+}-bearing silicate material (Clark, 1980), possibly akin to carbonaceous chondrites. Less than 2% of the latter would be required, given the high albedo of the rings in the 0.7–1.4 μm region (Clark and Lucey, 1984).

Voyager images revealed that the bright A and B rings, which dominate the rings' average spectrum, have much redder visual colors than the more neutral-colored C ring and Cassini Division (Estrada and Cuzzi, 1996). Subsequent modeling by Cuzzi and Estrada (1998) suggested that an initial few percent by mass of reddish organics might provide the reddening agent that dominates the properties of the optically-thick A and B rings, but that eons of meteoritic infall of dark, neutrally-colored material had polluted the less-massive C ring and Cassini Division, leading to their lower albedos and less-red visual colors.

Support for this latter interpretation was provided by Poulet and Cuzzi (2002) and Poulet et al. (2003), who fitted the regolith light-scattering model of Shkuratov (1999) to visible photometry acquired with HST (Cuzzi et al., 2002) and to new high-resolution near-infrared spectra obtained at the IRTF. In their best-fitting models, Poulet et al. (2003) invoke a ring particle regolith with ice grains ranging from 10 μm to 1 mm in size, containing inclusions of less than 1% of tholins[1] to provide the red color in the visible and intimately mixed with small but variable amounts of carbon grains to lower the albedo of the ice–tholin mixture. Ice–tholin mixtures have also been invoked to model the near-infrared spectra of the icy saturnian satellites (Cruikshank et al., 2005b).

To date, no spectroscopic evidence for ices other than H_2O has been reported for Saturn's rings, and no clearly diagnostic features of the non-icy component(s) have been identified, with the possible exception of a very weak absorption in the 0.8–0.9 μm region (Clark and McCord, 1980). Moreover, as neither Voyager spacecraft carried a near-infrared spectrometer, the spatial resolution of all existing near-IR spectra is limited to ∼6000 km (1 arcsec as seen from Earth). This is sufficient to separate the A, B and C rings (cf. Poulet et al., 2003), but not to look for spectral gradients within these major ring regions or to study the Cassini Division.

We report here on the first observations of Saturn's rings by Cassini's Visual and Infrared Mapping Spectrometer (VIMS), made shortly after the spacecraft's Saturn orbit insertion (SOI) burn on 1 July 2004. Although of modest spectral resolution compared with recent ground-based data sets, VIMS data provide the first near-infrared spectral observations of the rings that are capable of resolving much of their fine-scale structure. Free from the effects of telluric absorption, especially atmospheric water vapor, VIMS data also provide the first complete 1–5 μm spectra of the rings. Preliminary results were presented by Brown et al. (2006).

In this paper we present average visible and near-infrared spectra recorded by VIMS for the major ring regions, and describe both their regional and smaller-scale spectral variations. Simple comparisons of the observed radial brightness profiles with the predictions of single-scattering by a classical, many-particle-thick layer are made, but full radiative-transfer modeling of the observed spectra will be the subject of future work. After a brief overview of the VIMS instrument and the SOI observation sequence in Sections 2 and 3, we describe our data reduction procedures in Section 4. Section 5 presents a summary of the principal features seen in the data, which are then described in more detail in Sections 6 (radial profiles and single-scattering models) and 7 (spectral variations). Our principal results are summarized in Section 8.

[1] Tholins are the relatively refractory residue that results from the irradiation of a mixture of gases or ices containing simple hydrocarbons, nitrogen, and other components. Energy sources can be hard ultraviolet light, a microwave or coronal discharge, cosmic rays, or some combination of these sources. Analysis of tholins shows that they contain small aromatic and aliphatic hydrocarbons, as well as larger complex kerogen-like aromatic networks connected by aliphatic bridging units.

2. The VIMS instrument

The VIMS instrument is designed to obtain spatially-resolved reflectance spectra of planetary targets in the visual (hereafter VIS) and near-infrared (IR) wavelength range (0.35 to 5.10 μm). Details on the instrument design and calibration are provided by Brown et al. (2004); we summarize here the principal features and operational modes used at SOI. Between 0.35 and 1.05 μm, the VIS channel's long-slit spectrometer acquires data using a CCD array detector in 'pushbroom' mode, with a spectral resolution of 7 nm and a nominal spatial resolution of 0.5 mrad. A single-axis scan mirror is used to provide spatial sampling in the orthogonal or 'downtrack' direction, also at 0.5 mrad intervals. Between 0.85 and 5.10 μm, the IR channel's single-pixel spectrometer acquires data using an InSb linear array detector in 'whiskbroom' mode, with a spectral resolution of 16 nm. A 2-axis scan mirror provides images with a nominal spatial resolution of 0.5 × 0.5 mrad, matching that of the VIS channel. A full VIMS spectrum consists of 96 VIS spectral channels and 256 IR spectral channels and in the standard IMAGE operating mode these spectra are assembled into 'cubes' of up to 64 × 64 spatial pixels.

Several other operating modes are available and were employed in the SOI observations. For example, either or both VIMS channels can be operated in 'high resolution' mode, with the pixel sizes in the fast-scan or 'cross-track' direction reduced to 0.17 and 0.25 mrad, respectively. In LINE mode the motions of both the VIS and IR channel mirrors in the slow-scan direction are disabled and a single line of 64 pixels is acquired in the fast-scan direction. In POINT mode, the IR fast-scan mirror is also disabled and the IR channel stares in a fixed direction. In IMAGE and LINE modes the actual scan lengths are adjustable, up to a maximum of 64 pixels per line and 64 lines per image.

3. Observations

At approximately 3:07 Spacecraft Event Time (SCET) at Saturn on 1 July 2004, about 10 min after the successful completion of the 96-min main engine burn that placed Cassini in orbit around Saturn, the spacecraft executed a short turn to aim its suite of four optical remote sensing (ORS) instruments down at the rings. At the time, the orbiter was at a distance of ∼20,000 km above Saturn's cloud tops and a similar altitude above the unlit northern side of the C ring. Between 3:11 and 3:55 SCET, the ORS instruments obtained two continuous, high-resolution radial scans across the unlit side of the rings (see Fig. 1). Scan 1 covers the outer C and inner B rings at a radial resolution for the VIMS-IR channel of ∼15 km, while scan 2 covers the Cassini Division and the entire A ring at a resolution of 20–30 km. The solar incidence angle was 114°, while the emission angles were 47° for scan 1 and 63° for scan 2. Solar phase angles were 82° and 59°, respectively. Further geometric parameters are listed in Table 1.

For each of the two SOI radial scans, the ORS instruments stared in a fixed inertial direction rather than tracking any particular ring feature. Fig. 2 illustrates the variation of spacecraft to ring range, target radius and hour angle (measured in

Table 1
SOI observation geometry and instrument parameters

Parameter	Units	Scan 1	Scan 2	A ring mosaic
Geometric parameters				
Incidence angle	deg	114.5	114.5	114.5
Emission angle	deg	47.0	62.9	92–94
Phase angle	deg	82.2	59.3	123–136
Look direction[a]	deg	88–80	52–43	∼90
Spacecraft range	10^3 km	30–27	38–24	95–132
Ring radius	10^3 km	86.0–97.6	117.0–137.0	140–132
Ring longitude	deg	302–311	318–327	14–30
Radial velocity	km/s	16.9–16.6	14.5–10.8	
Azimuthal velocity[b]	km/s	1.0–2.1	4.5–5.2	
VIMS instrumental parameters				
Observation ID		RINGSCANG	RINGSCANA	ARINGLIT
Instr. mode		POINT	LINE	IMAGE
Cube size	pixels	64 × 64	64 × 1	12 × 12
IR integration time	ms	160	160	320
VIS integration time	s		10.0	3.84
Number of cubes		1	150	9
Number of spectra		4096	9600	
Start time, 2004 July 1	UT	3:11:00	3:27:00	4:54:30
End time, 2004 July 1	UT	3:24:00	3:54:30	5:15:30
Fast scan direction[c]	deg	103–95	69–60	
Radial resolution[d]	km	16–15	30–19	48–66
Sampling interval[e]	km	2.90–2.86	8.8–7.3	
Line spacing[f]	km		148–110	
IR line length[f]	km		416–359	
VIS line length[f]	km		277–239	

[a] Line of sight from the spacecraft to the rings, projected into the ring plane and measured from the radial direction in the direction of the rings' orbital motion.
[b] Relative to the ring material.
[c] Projected into the ring plane and measured from the radial direction in the direction of orbital motion.
[d] IR pixel size, projected on the radial direction in the rings.
[e] Approximate radial spacing between successive IR spectra.
[f] Radial components.

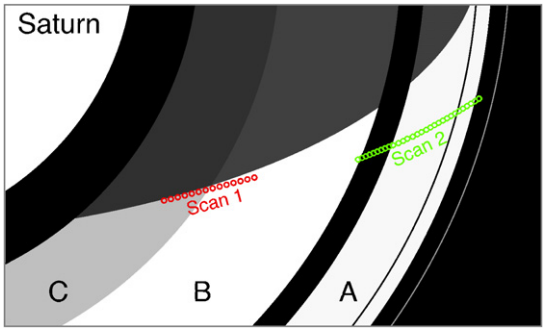

Fig. 1. Map view of the SOI ring scans, looking vertically down on the ring plane, with circles indicating representative positions of the target point projected onto the ring plane. The C, B, A and F rings are shown, as well as the narrow Encke gap in the outer A ring and Saturn's shadow cast across the rings. The Sun is to the left.

a prograde direction from the antisolar point on the rings) and VIMS-IR radial resolution as a function of time throughout the SOI observation period. The pointing of the ORS instruments was dictated by the need to obtain uninterrupted measurements of Saturn's magnetic field, while simultaneously maximizing the spatial resolution on the rings and avoiding the part of the rings within the planet's shadow. As a result, scan 1 was made roughly parallel to, and only ∼600 km outside, the edge of the planet's shadow across the C ring, as illustrated in Fig. 1.

Following the second radial scan, the spacecraft was reoriented in order to make in situ measurements of the neutral and ionized gas flow above the rings at 4:02–4:08 (Young et al., 2005; Tokar et al., 2005). During this brief period, the ORS instruments were pointed at the middle A ring at a range of less than 10,000 km (see Fig. 2); ISS images acquired at this time have revealed the signatures of several individual 100-m diameter moonlets (Tiscareno et al., 2006a), known as "propellors." Cassini was then placed in a 'safe' orientation to minimize the risk of damage due to particle impacts as the ring plane was crossed at 4:34 SCET at a radius of 158,500 km, between the orbits of the coorbital satellites Janus and Epimetheus and the G ring. Shortly afterwards, a series of oblique, high-phase-angle images of the sunlit side of the rings was taken from a range of ∼120,000 km. These highly foreshortened images cover the F ring and the outermost part of the A ring at a phase angle, $\alpha \simeq 130°$, and include the widely-reproduced image of the Encke Gap and associated wakes due to the satellite Pan. In this paper we will restrict our attention to the two high-resolution darkside scans.

During scan 1, the fast-scan direction projected on the rings was almost azimuthal and VIMS was operated in high-

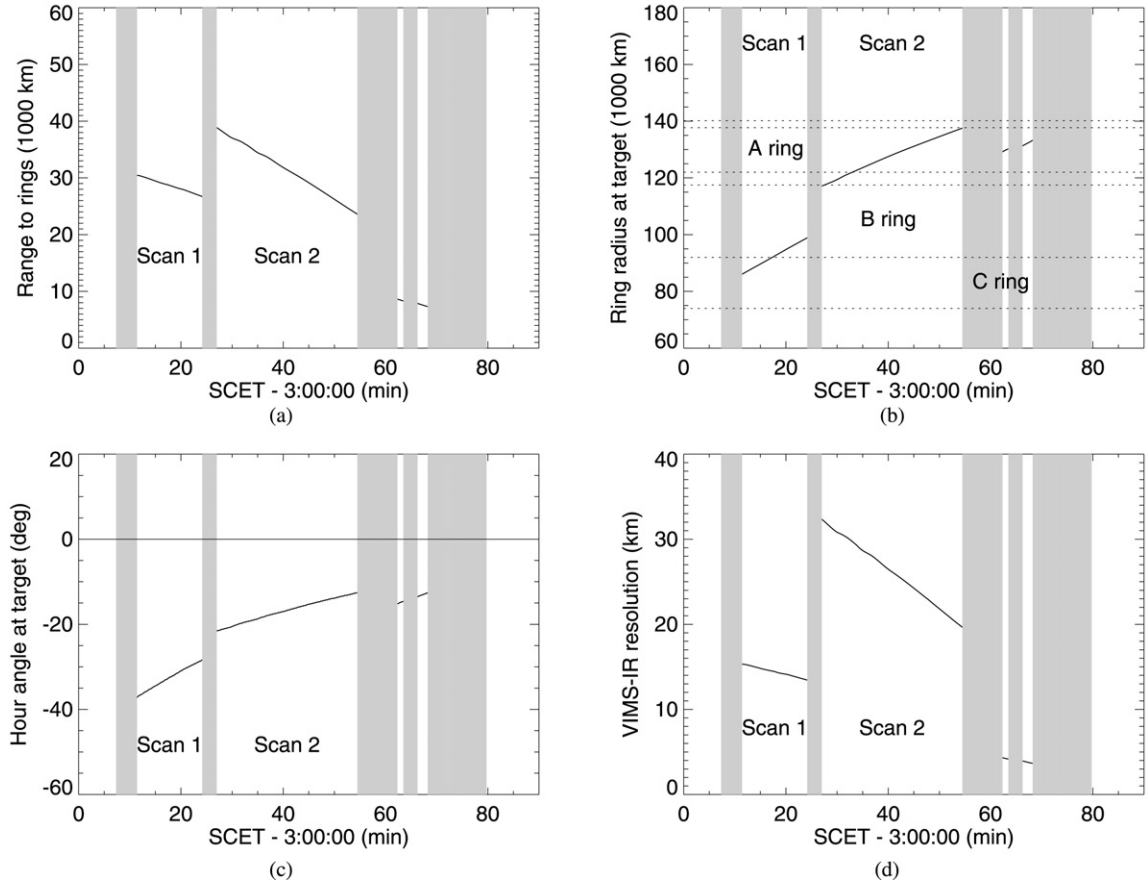

Fig. 2. Geometry of the Cassini SOI observations as reconstructed from engineering telemetry and navigation data, as functions of spacecraft event time (SCET) on 1 July 2004, which is UTC as measured at Saturn. Vertical grey bars indicate spacecraft turns. The individual panels show (a) range from Cassini to the target location on the rings, (b) radius of the target point in the ring plane, (c) hour-angle of the target point in the ring plane, measured in a prograde direction from the antisolar direction, and (d) the VIMS-IR radial resolution. Two short segments between 60 and 70 min show the VIMS pointing during the period of plasma observations (Tokar et al., 2005). Horizontal dotted lines in the second panel delineate the major ring regions, A, B and C, plus the F ring. Cassini crossed the ring plane at approximately 94 min.

resolution POINT mode, with a nominal IR integration time of 160 ms. The average interval between samples was 162.75 ms, with a brief gap of 423 ms to measure the instrumental background level after every 64 samples. The IR channel stared in a fixed inertial direction as the spacecraft's orbital motion carried the instrument boresight across the rings at an average radial velocity of ∼17 km/s. In this mode, which is designed primarily for stellar occultation experiments, each IR spectrum is precisely time-tagged but no data are acquired by the VIS channel. A total of 4096 IR spectra were obtained over a period of ∼11 min, at an average radial sampling interval of 2.9 km. However, the actual radial resolution of the data is set by the projected pixel size of ∼15 km (see Table 1).

For the second SOI scan, the roll attitude of the spacecraft was such that the VIMS fast-scan direction had an outward radial component and the instrument was operated in high-resolution LINE mode, acquiring both VIS and IR data. As in the first scan, the inertially-fixed instrument boresight was carried across the rings by the spacecraft's orbital motion, resulting in a series of overlapping 64-pixel long diagonal line segments being 'painted on' the rings. The nominal IR integration time was again 160 ms per pixel, with a sampling interval of 162.75 ms and an interline delay of 491 ms for backround measurements. The VIS integration time was ∼10.0 s per line, plus an interline delay of 895 ms for array readout and synchronization with the IR channel. A total of 150 lines was obtained over a period of 27.5 min, with average lengths, projected onto the radial direction in the ring plane, of 260 km (VIS) and 390 km (IR). (See Table 1 for further details.) With an average radial spacing between successive line centers of ∼130 km, this provides significant overlap between adjacent lines and permitted complete radial scans of the Cassini Division and A ring to be assembled for both VIS and IR data. As for scan 1, the radial resolution of the IR data is set by the projected pixel size of ∼25 km. For the VIS data the instantaneous spatial resolution is ∼5 km per hi-res pixel, but the effective radial resolution is limited by smear during each 10 s integration and varies from ∼150 km to ∼110 km across the scan (see Table 1).

Both scans were quasi-radial, covering only a limited range of ∼9° in longitude on the rings. Because of the unusually close target range at SOI, the observations presented here are likely to have the highest spatial resolution of any ring reflectance observations acquired by VIMS during Cassini's four-year orbital tour of the Saturn system.

4. Data analysis

4.1. Flux calibration

4.1.1. IR data

Standard calibration of VIMS-IR imaging data involves four steps (McCord et al., 2004). First, an internal background spectrum, recorded at the end of each line of data and due primarily to thermal emission from the instrument, is subtracted from each raw spectrum. Next, a flat-field correction is applied to correct for slight variations in response with scanning mirror position and a despiking algorithm is used to identify and flag spikes due to cosmic rays and gamma rays from the radioisotope thermal generators on the spacecraft. Finally, a wavelength-dependent calibration factor is applied to convert the corrected data values to I/F, or target reflectance.[2] This final correction is based on a combination of pre-launch calibration measurements and post-launch observations of the Moon, Venus and the Galilean satellites, and employs a solar reference spectrum to convert absolute fluxes to reflectance. For further details, see McCord et al. (2004). The specific calibration file used for the data presented here was designated RC15, and represents our best knowledge at the time of writing.

For the LINE mode data of scan 2, the above steps were carried out using the standard VIMS pipeline calibration procedure developed by the science team. Small differences in I/F for the same ring radius seen in different pixels of adjacent lines revealed the need for an additional flatfield correction, amounting to 4% across each line between 1.0 and 1.5 μm but decreasing at longer wavelengths.

For the POINT mode data of scan 1, only the background-subtraction and I/F calibration steps were carried out. For such data, flat-fielding is unnecessary and the standard cosmic ray detection algorithms fail, as they depend on comparisons between neighboring spatial pixels.

4.1.2. VIS data

The calibration procedure for VIS data is extensively described in previous papers (Coradini et al., 2004; McCord et al., 2004; Filacchione et al., 2007). The current calibration pipeline for the VIS channel is based on both ground-calibration and in-flight data: spectral calibration is estimated from pre-launch measurements conducted by Officine Galileo (now Selex-Galileo Avionica); in-flight data for Mare Crisium on the Moon are used for radiometric calibration; and the flat-field matrix was derived using observations of Venus' atmosphere.

After correction for a constant electronic offset, the raw VIS data are converted to I/F by applying the standard instrumental transfer function, which includes both the flat field correction and spectral calibration. Spikes due to cosmic rays passing through the CCD detector are common in cubes obtained with long exposure times (>1 s) and are corrected with a standard de-spiking algorithm using a $3 \times 3 \times 3$ kernel and a 1.7-σ cut-off level. In the final step, small sky background and electronic readout offsets (which vary from pixel to pixel and across the spectrum, but are constant from line to line) were subtracted using the last line of the scan, acquired while the instrument was looking at empty sky outside the A ring, but with the same integration time and operating mode used for the ring observations.

4.2. Geometric reconstruction

As both radial scans were carried out with the VIMS boresight pointed in a nominally-fixed inertial direction, a determination of the location in radius and longitude of each VIMS pixel depends primarily on accurate knowledge of the spacecraft trajectory. This was reconstructed after the fact by the Cassini Navigation team using ground-based Doppler tracking and ranging data. However, during the post-SOI science period the spacecraft attitude was controlled by thrusters, rather than the more stable reaction wheels normally employed, resulting in slow, aperiodic oscillations in the actual pointing direction. Using telemetry from the onboard gyros plus a pair of redundant star trackers, the actual pointing profile was reconstructed by the Cassini Attitude Control System team.

Starting with the reconstructed trajectory and spacecraft pointing profile, and the known location of the VIMS boresight vector in the spacecraft's internal coordinate system, we predicted the instantaneous position of the VIMS boresight projected into Saturn's ring plane. For scan 2, an additional, time-variable offset of the instantaneous look direction was required to account for the motion of the IR fast-scan mirror as it traced out each line of data. Correlation of the data from adjacent lines showed that, in order to match up ring features between scan lines, the calculated IR radial scan lengths needed to be adjusted by a factor which varied linearly from +0.5% in the Cassini Division to −3% in the outer A ring. This correction is probably due to a small rotation of the instrument's field of view, as projected onto the rings, relative to the anticipated orientation listed in Table 1.

Comparison of the resulting radial I/F profiles with the optical depth profile of the rings measured by the Voyager photopolarimeter experiment, as geometrically reconstructed by Nicholson et al. (1990), showed systematic differences in the radii of well-known and sharp-edged ring features which varied smoothly from ∼100 km in the C ring to ∼50 km in the A ring. Errors at this level are expected to arise from uncertainties in the reconstructed spacecraft attitude, and are much larger than the intrinsic uncertainties of ∼1 km in the absolute radii of such ring features, as determined from Voyager and ground-based occultation observations (French et al., 1993). We have therefore estimated the necessary radial corrections to the SOI data by cross-correlating sections of the IR profiles with the PPS optical depth profile, and then modeling these errors using a 4th-order polynomial fit for each scan. The rms residuals between feature radii in the PPS and corrected VIMS data are ∼5 km, or about one-third of our radial resolution. The final step for the IR data was to rebin the overlapping line-mode data from scan 2 onto a regular grid of 2001 spectra at 10 km inter-

[2] I/F is defined as the ratio of the ring's surface brightness to that of a perfect Lambert reflector oriented at normal incidence.

vals in radius, starting at 117,000 km. A similar 4001-point file was also generated at 5 km intervals.

The VIS data for scan 2, acquired as a series of 150 64-pixel lines, were first reprojected onto a 2-dimensional spatial reference grid of 610 × 807 pixels using the same reconstructed trajectory and spacecraft pointing profile. Each pixel was assigned a radial distance in the ring plane, which was then used to sort the 9600 individual spectra into a 2-dimensional radius-wavelength array. Although radial smear during each 10 s integration amounted to between 150 and 110 km, successive spectra are offset radially by only ∼2.0 km on average, resulting in a very large oversampling factor. Therefore, by applying a moving average over 75 samples, we were able to improve significantly the signal-to-noise ratio of these data without sacrificing spatial resolution.

5. Overview of the data

We organize our discussion of the VIMS SOI data as follows. In this section we present average spectra for the classical A, B and C rings, plus the Cassini Division, with qualitative interpretations in terms of ice grain size and possible non-icy contaminants; radial profiles of I/F extracted from the IR data; and an overview of the large-scale spectral variations seen in the data. In Section 6 we examine the radial I/F profiles in some detail, drawing comparisons between the VIMS SOI data and optical depth and brightness profiles obtained from Voyager observations. We also present a simple radiative transfer model for the observed I/F profiles based on the assumption of single-scattering in a many-particle thick ring. In Section 7 we investigate the radial variations in the infrared spectra of the rings on both regional and local scales.

5.1. Average ring spectra

Average spectra for the four classical ring regions derived from the VIMS SOI data are shown in Fig. 3, where we have combined VIS and IR data when both are available. These spectra are quite similar to the ground-based reflectance spectra of the A, B and C rings obtained by Poulet et al. (2003), but we caution the reader that the SOI spectra were taken under conditions of diffuse transmission, a geometry which differs significantly from that which applies to all published Earth-based and HST spectroscopy. The large sizes of typical ring particles—estimated at a few centimeters to several meters in the main rings (Marouf et al., 1983; French and Nicholson, 2000)—means that individual ring particles are almost certainly completely opaque at visual and near-infrared wavelengths. Thus while VIMS was observing sunlight transmitted through the rings at SOI, most of the photons were undoubtedly *reflected* by individual ring particles and the spectra discussed here are better thought of in terms of reflectance spectra of "partially-

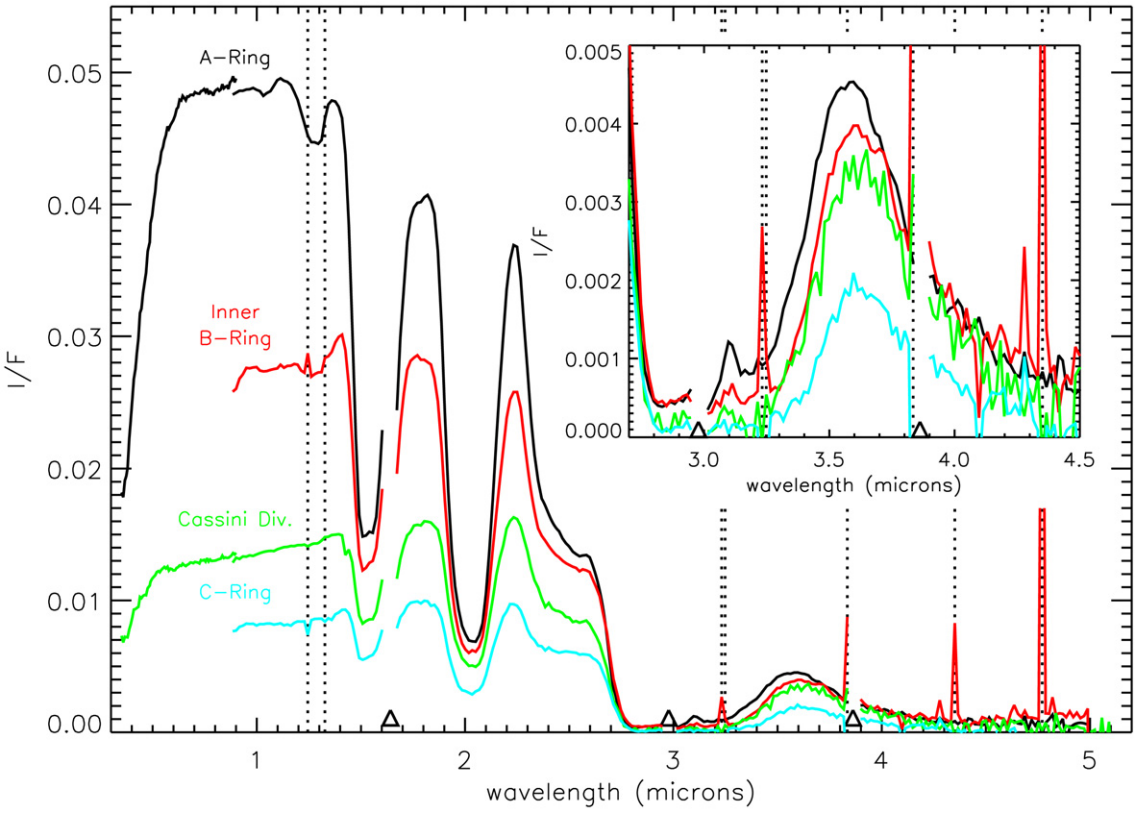

Fig. 3. Average spectra for the A, B and C rings as well as the Cassini Division derived from the VIMS SOI data. The region around the strong water ice fundamental at 3.1 μm is enlarged in the inset. Triangles indicate gaps between the IR focal plane blocking filters where the spectra may be unreliable; these channels have been suppressed here. Vertical dotted lines indicate hot pixels, which can saturate in long integrations. Data from the VIS channel were acquired only for scan 2, covering the Cassini Division and A ring, and have been cropped at 0.85 μm because of residual calibration problems at the longest wavelengths.

illuminated moonlets" rather than as conventional transmission spectra. Although there must be a small contribution from light transmitted through the particle regoliths, subsequent observations by VIMS of the sun seen through the rings confirm that, in pure transmission, the main rings appear as a spectrally featureless grey screen.

In most cases, the statistical measurement errors in raw VIMS-IR spectra due to detector read noise, dark current and photon statistics are negligible. The digitization level of the data, or 1 data number (DN), corresponds to ∼300 detected photoelectrons and is approximately equal to the RMS read noise level. Thermal background in the spectrometer, though substantial at longer wavelengths, results in a noise level which should also barely rise to the 1 DN level. However, the very low reflectance of the rings at wavelengths beyond 3 μm combined with the darkside viewing at SOI, short integration time and the rapidly-decreasing solar flux at these wavelengths results in the typical signal in a single pixel being only a few DN beyond 3 μm. Empirical estimates of the RMS noise in the SOI data, as measured in regions of the A and B rings where the reflectance is almost constant over a few hundred km, yield 1-σ uncertainties in I/F of 0.0001–0.0002 between 1.0 and 3.0 μm, increasing to 0.0004 at 4.0 μm and 0.0012 at 5.0 μm. These numbers were computed at a radial sampling interval of 10 km, equivalent to averages over 3–4 raw pixels and, as expected, correspond to ∼0.5 DN at each wavelength. The noise level in the spectra in Fig. 3 is only slightly less than this, despite the fact that they are averaged over several hundred radial bins, a situation we attribute to low-spatial-frequency $(1/f)$ noise in the rings and/or the instrument.

The statistical errors in the averaged VIS spectra, where the sun is much brighter and the ring reflectance is high, should also be quite small but there remain some unresolved issues in the calibration of the VIS data at longer wavelengths and we have preferred to use the IR data in the overlap region between 0.85 and 1.10 μm.

5.1.1. Water ice

The VIMS SOI spectra of all parts of Saturn's rings are dominated by fine-grained water frost, consistent with previous ground-based observations (Pilcher et al., 1970; Lebofsky et al., 1970; Clark and McCord, 1980; Poulet et al., 2003). Generally speaking, the ice bands are strongest in the A ring, weakest in the C ring and of intermediate strength in the inner B ring and the Cassini Division. In addition to the strong bands centered at 1.5, 2.0, 2.9 and ∼4.5 μm, which are readily apparent in all four ring regions, the weaker overtone bands of water ice first reported by Clark (1980) at 1.04 and 1.28 μm are seen clearly in the A ring and weakly in the inner B ring. We note that laboratory experiments show that even tiny amounts of absorbing, non-icy material will quickly suppress these weak bands (Clark, 1981a, 1982; Clark and Lucey, 1984), implying that the ice covering the surfaces of particles in the A and B rings, at least, is quite clean. In the VIMS spectra of the C ring and Cassini Division, on the other hand, these overtone bands are not detectable. This is consistent with a larger fraction of absorbing, non-icy material in these regions, and thus with similar inferences drawn from regional variations in the broadband colors of the rings at visual wavelengths by Cuzzi and Estrada (1998).

Based on light-scattering models fitted to high-resolution, ground-based 0.3–4.0 μm data, Poulet et al. (2003) found that a combination of several different grain sizes of water frost was necessary to match the rings' spectra, with a range of ∼10 μm to 1.4 mm providing the best match to the A and B rings. This is consistent with the earlier models of Pollack et al. (1973) and Clark et al. (1986). Surprisingly, Poulet et al. (2003) also observed relatively strong 1.04 and 1.28 μm bands in the C ring, which they fitted by a model with grain sizes between 30 μm and 7.5 mm.

Comparison of the 1–2.5 μm region of the VIMS spectra with laboratory spectra of water frost (see, e.g., Clark, 1981a, 1981b or Fig. 4) shows clearly that the average regolith grain size must be less than about 100 μm in all regions. A strong constraint is provided by the broad reflection peak at 3.6 μm, which is prominent only for quite fine-grained surfaces. This feature is defined by strong flanking absorptions at 2.9 and ∼4.5 μm, and disappears completely for solid ice or for frosts with grain sizes which exceed ∼100 μm (Clark, 1981a; Clark and Lucey, 1984). Comparing the 1.0–5 μm region of the VIMS spectra in Fig. 3 with the series of model ice spectra in Fig. 4 (see Hansen and McCord, 2004 for details), we conclude that a significant fraction of grains in all four major ring regions must lie in the radius range $5 < r_g < 20$ μm, with somewhat smaller sizes indicated in the C ring and Cassini Division in comparison with the A and B rings. Although comparisons with ice spectra computed independently using models based on Hapke and Shkuratov theories, as well as different sets of optical constants, show small variations in the shapes and depths of the bands, the basic conclusion that the rings' spectra are best fit by an average grain diameter of 10–40 μm appears to be robust. This is also consistent with previous estimates of 30 μm by Clark et al. (1986) and $r_g = 20$ μm by Doyle et al. (1989).

Nestled within the broad and very strong water ice fundamental band at ∼2.9 μm is a narrow reflectance peak at 3.10 μm, due to front-surface reflections from opaque ice grains.[3] In the VIMS SOI data, this "Fresnel peak" is seen quite clearly in the A ring (see inset in Fig. 3), but is much weaker or absent in the C and inner B rings as well as the Cassini Division. Although insensitive to grain sizes larger than a few microns (see Fig. 4), this spectral feature differs in its strength and shape between crystalline and amorphous ice (Hansen and McCord, 2004). Unfortunately the Fresnel peak in the SOI data is too weak to permit any strong conclusions to be drawn on this point. The reason for such a weak Fresnel peak is unclear, but possible explanations include either the moderate phase angle at SOI or absorption at this wavelength by another compound (e.g., NH_3) that has so far eluded detection. Hansen et al. (2005) have noted that saturnian icy satellites also exhibit rather weak Fresnel peaks relative to those of the Galilean satellites.

[3] The absorption coefficient of water ice is a maximum at 3.08 μm, while the refractive index reaches a minimum at ∼2.95 μm. The latter controls the location of the broad reflectance minimum (Clark et al., 1986).

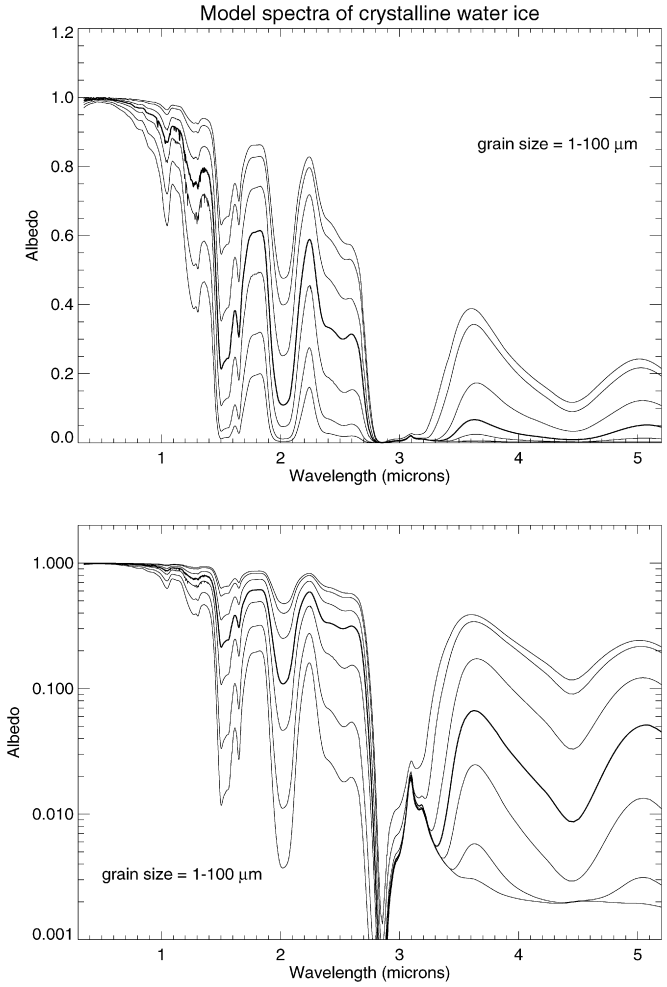

Fig. 4. Model reflectance spectra for opaque layers of crystalline water ice particles at a temperature of 110 K and grain radii, $r_g = 1$, 2, 5, 10, 20, 50 and 100 μm, displayed in both linear and logarithmic units. Smaller grain sizes correspond to generally higher albedos and weaker spectral features, except in the vicinity of the narrow Fresnel peak at 3.10 μm. The best overall fit to the SOI spectra of Saturn's A and B rings is for a radius of 10 μm, indicated by the heavier line. Note that the broad 3.6 μm peak disappears for grain radii of ∼100 μm and larger. For details of the model calculations, which are based on a δ-Eddington two-stream model and optical constants measured by Grundy and Schmitt (1998), Bergren et al. (1978) and Clapp et al. (1995), see Hansen and McCord (2004).

5.1.2. Non-ice features

We see no spectral features due to other ices that might be stable at the ring's temperature of ∼90 K, such as NH_3 or its mono- and dihydrates at 2.20 and ∼3.5 μm, CO_2 at 4.27 μm or SO_2 at 2.55 and 4.05 μm. We can also rule out significant amounts of simple alcohols such as CH_3OH at 2.27 μm and organics with C–H stretching fundamentals at 3.3 to 3.5 μm. We also see no evidence for the 2.42 μm feature identified in VIMS spectra of dark regions on Phoebe, Iapetus, Dione, and Hyperion (Clark et al., 2005b, 2005a, 2005c). It is possible that some of these materials (or even CH_4 or CO, which are quite volatile in their pure forms at saturnian temperatures) might be present in small abundances ($\leqslant$2%) or as clathrates, as the latter are spectrally almost indistinguishable from pure H_2O ice at our resolution. Quantitative upper limits will eventually be derived from higher signal-to-noise spectra of the sunlit side of the rings.

Although H_2O dominates the near-IR spectra of the rings, their steep decline in reflectance shortward of about 0.6 μm must be due to something else [see, e.g., Esposito et al. (1984) for a review of ground-based observations of the rings' visible spectrum]. Although early interpretations focused on silicate and/or sulfur-bearing minerals as the most likely coloring agents, recent studies of the rings' visible and near-IR spectra have identified tholins—reddish, organic-rich, refractory materials suspected to be present in the atmosphere of Titan and on the surfaces of many red outer Solar System bodies, such as Pholus (Wilson et al., 1994; Cruikshank et al., 1998, 2005a)—as the most likely agents responsible for the distinctly reddish color of the rings at visual wavelengths. In a study of the color of Saturn's rings, Cuzzi and Estrada (1998) found that the particles in the A and B rings contain a material which imparts a distinct red color, while the particles in the C ring and Cassini Division are lower in albedo and less red in color. They note that "No silicates have the appropriate combination of steep spectral slope and high absorptivity to explain the rings' visual color while remaining compatible with microwave observations." Titan tholin matches the colors and albedos of the particles when incorporated into the H_2O ice grains. To explain the lower albedo and more neutral color of the darker rings, Cuzzi and Estrada (1998) suggest that "material with properties like carbon black, as seen in at least some comets and interplanetary dust particles, is needed."

Subsequent modeling of the rings by Poulet and Cuzzi (2002) and Poulet et al. (2003) also incorporated tholins and amorphous carbon to achieve fits to the observational data in the 0.3–4.0 μm range. Poulet et al., concluded further that, for the A and B rings, while the carbon grains are intimately mixed in a "salt and pepper" fashion with the ice, the tholins are mixed at the molecular level within the ice grains themselves. (In the C ring, however, their best-fitting model consists of a mixture of crytalline water ice grains of three different sizes, some of which contain molecular inclusions of both tholins and amorphous carbon.) Unfortunately, tholins exhibit relatively few and weak absorption features in the VIMS near-IR region (Cruikshank et al., 2005a), except at wavelengths near 3.0 and ∼4.5 μm where water ice is also highly absorbing. Thus we have not so far found specific supporting evidence for tholins in the infrared portion of the VIMS SOI spectra.

VIMS spectra of the Cassini Division and the C ring show a distinct reddish continuum slope between 0.5 and 1.4 μm, perhaps extending as far as 2.2 μm, which is not characteristic of pure water ice, which tends to have a blue continuum slope in this region (see Fig. 4). This continuum slope might be due to the same Titan tholins invoked by Poulet and others to explain the steep decrease in reflectance shortward of 0.6 μm, as illustrated in the spectra shown by Cruikshank et al. (1998). The outer C ring also appears to show a very broad, shallow absorption centered near 1.2 μm, which is seen more clearly in the regional C ring spectra shown in Fig. 25 below. A similar but stronger absorption is seen in VIMS spectra of Saturn's irregular moon Phoebe (Clark et al., 2005a) and of several of the icy

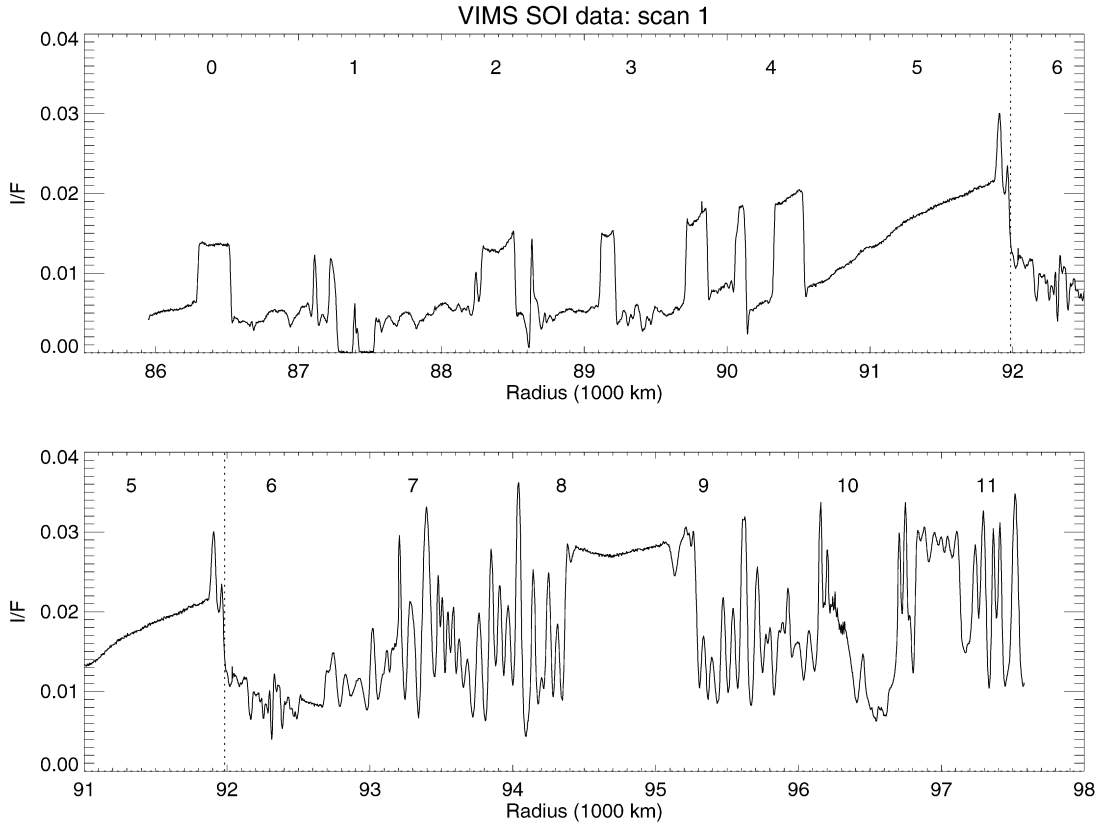

Fig. 5. Radial I/F profile of the unlit side of the C and B rings at 1.08 μm, derived from the first VIMS SOI scan. Numbers indicate the central radii of ISS narrow-angle camera images, each of which spans ∼200 km in radius (Porco et al., 2005). The vertical dotted line at the outer edge of the 'ramp' indicates the conventional boundary between the C and B rings.

regular satellites, notably Dione (Clark et al., 2007), where it is attributed to silicate minerals. Although the C ring feature could also be due to an Fe^{2+}-bearing silicate mineral such as olivine (Clark, 1999; Clark et al., 2003), its weak and indistinct nature makes a definite conclusion or specific identification problematic. VIMS observations of the narrow F ring also show a broad absorption centered near 1.2 μm, but only at high phase angles. Subsequent VIMS observations show that the C ring spectrum in this region varies considerably with phase angle, suggesting the possibility that this absorption is actually due to a previously unreported scattering characteristic of micron-sized water ice grains. A definite identification of this feature must await additional phase angle coverage of the rings, perhaps supplemented by new laboratory work on the phase angle dependence of water frost spectra.

5.2. Ring structure

A different perspective on the VIMS SOI data is provided by Figs. 5 and 6, where we plot radial profiles of the ring's I/F at a wavelength of 1.08 μm. This is a continuum wavelength where the signal-to-noise ratio of the data is at its highest, but most other wavelengths yield essentially identical profiles. For future reference, we briefly identify here the more prominent ring features seen in these profiles. As noted above, the statistical uncertainty in the I/F at this wavelength is at most 0.0002, which is almost invisible on the scale of these figures.

In addition to several 100 to 250 km-wide 'plateau' features, the outer C ring in Fig. 5 is dominated by the Maxwell gap and its embedded eccentric ringlet at 87,500 km (Porco et al., 1984a) as well as two narrower gaps and their associated ringlets at 88,700 and 90,200 km, discussed by Porco and Nicholson (1987). The C ring's outer 'ramp' between 90,600 and 91,800 km serves as a transition into the inner B ring, which is usually considered to begin at 92,000 km.

In the SOI geometry of diffusely-transmitted sunlight, the inner B ring is not much brighter than the outer C ring and is considerably fainter than the adjacent ramp. This region is characterized by two relatively homogeneous zones (informally referred to as 'flat spots') at 94,400–95,250 and 96,850–97,100 km, embedded within a wider zone of irregular, oscillatory structure with a characteristic wavelength of ∼80 km (Horn and Cuzzi, 1996). The high-frequency structure near 96,300 km is due to the strong Janus 2:1 density wave (Holberg et al., 1982) but this is barely resolved in the VIMS data.

At the beginning of the second scan in Fig. 6 we see the outermost 500 km of the B ring, bounded at ∼117,600 km by the Huygens gap with its embedded eccentric ringlet (Turtle et al., 1991). The Cassini Division harbors several other gaps at radii of 118,250, 118,600, 118,950 and 119,900 km, discussed by Flynn and Cuzzi (1989) and Nicholson et al. (1990), but only the last—the Cassini Outer Rift—is well resolved in the VIMS scan. The outer half of the Cassini Division has a very different appearance, dominated by a curious triple-peaked band at

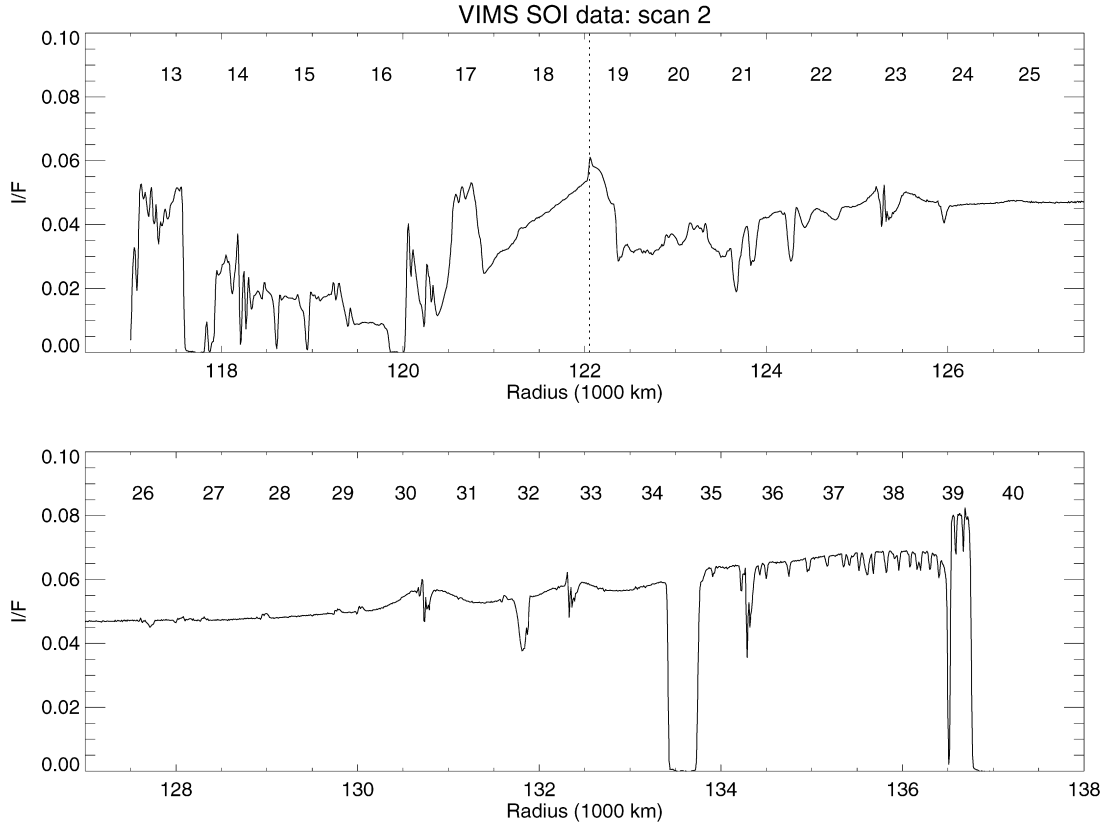

Fig. 6. Radial I/F profile of the unlit side of the Cassini Division and A ring at 1.08 μm, derived from the second VIMS SOI scan. Numbers indicate the central radii of ISS narrow-angle camera images, each of which spans ∼200 km in radius (Porco et al., 2005). The vertical dotted line at the outer edge of the 'ramp' indicates the conventional boundary between the Cassini Division and the A ring.

120,700 km and a thousand-km wide ramp that marks the conventional transition to the inner A ring at 122,000 km and which is analogous in many respects to the ramp that terminates the C ring.

Except for its innermost 3000 km, the A ring's I/F profile is relatively smooth, punctuated only by narrow dips due to the numerous unresolved density and bending wavetrains associated with the many satellite resonances in this region (Lissauer and Cuzzi, 1982). Most prominent in the VIMS data are the density waves driven at the Janus/Epimetheus 4:3 (125,350 km), 5:4 (130,750 km) and 6:5 (134,300 km) inner Lindblad resonances, as well as the Mimas 5:3 bending wave (131,800 km) and density wave (132,400 km) pair. In the outer A ring the 325 km-wide Encke Gap centered at 133,600 km is the most prominent feature, followed by the much narrower Keeler Gap at 136,500 km.

Note that the transitions from the C ring ramp to the B ring in Fig. 5 and from the Cassini Division ramp to the A ring in Fig. 6 are both accompanied by abrupt *decreases* in I/F, although the optical depth increases substantially at both locations. As discussed further in Section 6, this is a consequence of our viewing the rings at SOI in diffusely-transmitted rather than reflected light.

Also shown in Figs. 5 and 6 are the center radii of the ISS narrow-angle camera images taken during the SOI scans. These 1024 × 1024 pixel images have spatial resolutions of ∼200 m per pixel (Porco et al., 2005), but with an average radial spacing of 700–1000 km their radial coverage is incomplete, unlike the continuous but lower-resolution VIMS scans.

5.3. Spectral variations

While spectra and radial I/F profiles reveal different aspects of the rings, the true value of the VIMS SOI data lies in its unprecedented *combination* of spatial and spectral information. In Figs. 7–9 the VIMS data are presented in an image format, with ring plane radius on the horizontal axis and wavelength on the vertical axis.

In the upper panel of Figs. 7 and 8 the calibrated near-IR spectral reflectance profiles are shown. To first order, the radial variations in ring brightness are controlled by optical depth variations, as explored further in Section 6 below, and are very similar at all wavelengths. Although the near-IR spectrum of the rings is rather homogeneous, there are many subtle variations in the spectrum across the rings. These are better illustrated in the lower panels of Figs. 7 and 8, where the individual spectra have first been divided by the average spectrum of all spatial samples in the scan, and then normalized to a common brightness level over the range 0.85–1.70 μm. This presentation highlights radial variations in the reflectance spectrum, while suppressing the distracting, large-scale brightness variations associated with the radial optical depth profile and possible variations in particle albedo. Pronounced variations are now revealed in the

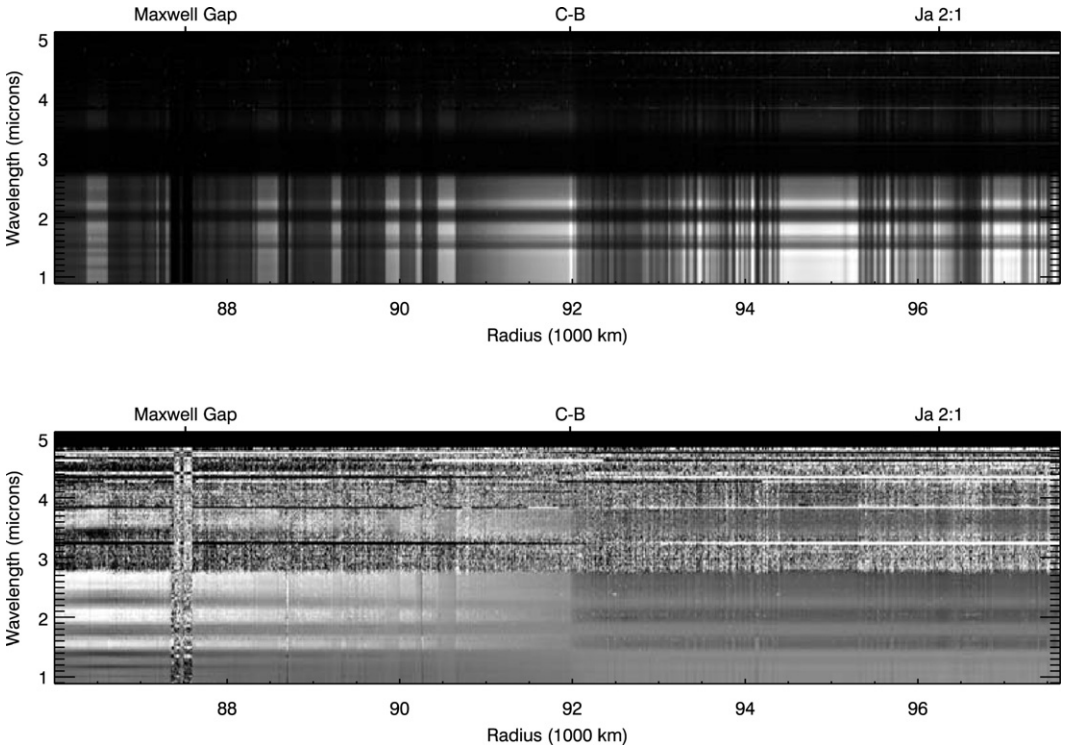

Fig. 7. Spectra from the first VIMS SOI scan are shown in image format as functions of ring plane radius and wavelength. Calibrated IR spectra are shown in the upper panel, with dark horizontal bands showing the strong ice bands centered at 1.5, 2.0 and 2.9 μm. In the lower panel these same data have been first divided by the grand average of all 4096 individual spectra, and then normalized to a common brightness level averaged over the first 50 spectral channels (0.85–1.7 μm). This procedure suppresses both the average spectral shape and brightness variations due to radial optical depth variations, leaving only the relatively subtle deviations in the spectrum from region to region. Labels along the top of each plot identify prominent ring boundaries, gaps, and strong density waves.

strengths of the water ice bands at 1.5 and 2.0 μm across the rings.

In Fig. 7 we see that the 1.5 and 2.0 μm bands change gradually from bright horizontal stripes (i.e., weaker than average absorption) in the outer C ring to dark stripes (i.e., stronger than average absorption) in the inner B ring. Most of this shift occurs across the "ramp" in the outer C ring. In Fig. 8 we see that the same ice bands change abruptly from neutral (i.e., average absorption) in the outermost B ring to bright horizontal stripes (i.e., weaker than average absorption) in the Cassini Division, and then gradually to dark stripes (i.e., stronger than average absorption) in the middle A ring. Although part of this shift occurs across the outer half of the Cassini Division, a significant gradient persists across the inner 4000 km of the A ring. Both 1.5 and 2.0 μm bands weaken slightly outside the Encke Gap and then much more dramatically beyond the Keeler Gap.

More subtle are several dark absorption bands at 1.00, 1.15, 1.35, 1.75, and 2.3 μm, which appear only in the C ring (see Figs. 7 and 25). All five of these bands are characteristic of materials containing C–H bonds. They are strongest interior to the Maxwell Gap at 87,500 km and gradually fade out at larger radii. (A sixth band at 3.4 μm is seen when spectra from different radii are ratioed to remove the strong water ice absorption at this wavelength, and is also found to fade beyond the Maxwell Gap.) Both the plateaux and low-optical-depth background regions show similar band depths. The wavelengths and relative strengths of these 'organic bands' match closely those of methane bands in Saturn's spectrum and, based on the close proximity of the track of scan 1 across the rings to the edge of Saturn's shadow (cf. Fig. 1), we conclude that the most likely source of these features in the SOI data is CH_4 absorption in Saturn's upper atmosphere. At a radius of 87,000 km, light rays from the Sun en route to the rings penetrated to a minimum altitude of only ∼425 km above the 1 bar level on Saturn, corresponding to a pressure level of ∼0.05 mbar. Radiative transfer calculations using both line-by-line and correlated-K calculations smoothed to the VIMS spectral resolution of 17 nm predict fractional absorptions of 15–20% in the 1.15–2.3 μm methane bands for rays which graze the planet's limb at this altitude, comparable to what is seen in the SOI spectra. Hence these features are unrelated to the rings.

Fig. 9 presents the VIS data for scan 2 in a similar format. In the upper panel is shown a series of calibrated I/F spectra, each extracted at the center of a line (sample 32), arranged in order of increasing radius. Despite the lower radial resolution of the VIS data, all the major features in the Cassini Division and A ring noted in Fig. 8 can be readily identified. This includes the Huygens Gap and Outer Rift in the Cassini Division, the Encke Gap, and the unresolved Keeler Gap, as well as the strong density and bending waves due to Mimas and the coorbital satellites, Janus and Epimetheus. Under the diffuse-illumination conditions of the SOI scan, the outer regions of the A ring (outside the Encke gap) are substantially brighter than the rest of the A ring or even the outermost B ring.

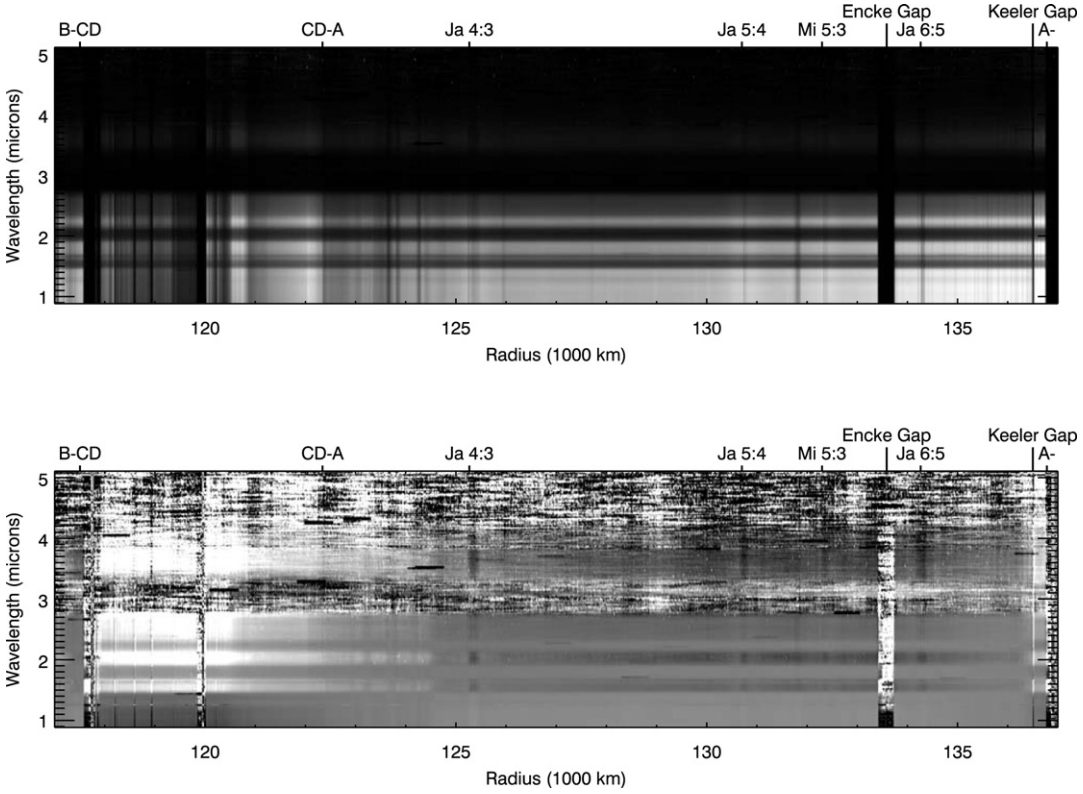

Fig. 8. Spectra from the second VIMS SOI scan are shown in the same format as in Fig. 7. Again, calibrated IR spectra are shown in the upper panel, with dark horizontal bands representing the strong ice bands centered at 1.5, 2.0 and 2.9 μm. In the lower panel these same data have been first divided by the grand average of all 2001 individual spectra, and then normalized to a common brightness level averaged over the first 50 IR spectral channels (0.85–1.7 μm). Labels along the top of each plot identify prominent ring boundaries, gaps, and strong density waves.

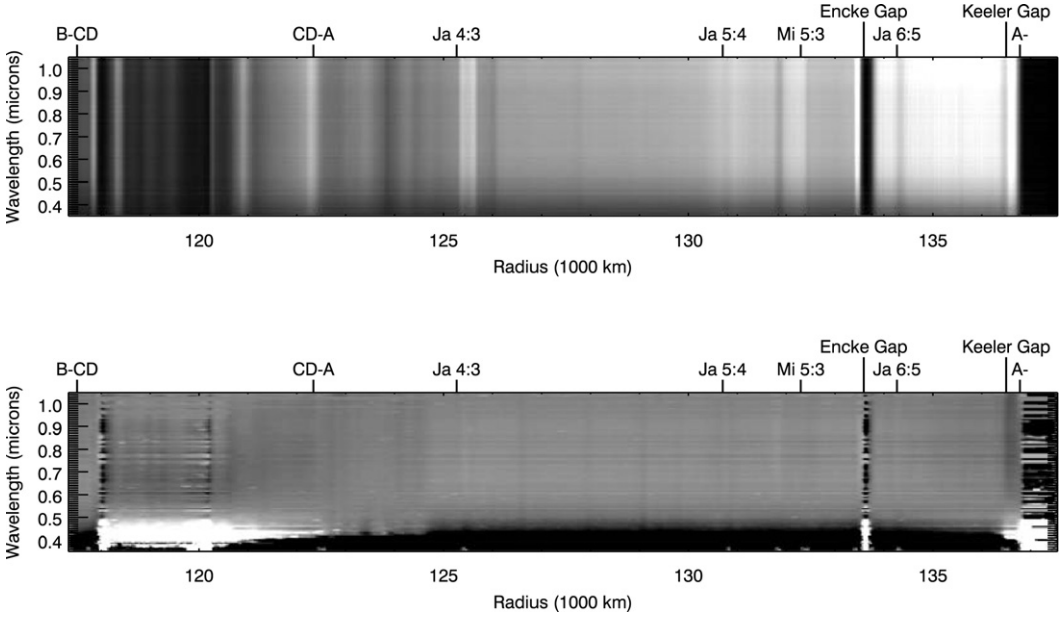

Fig. 9. VIS spectra from the second VIMS SOI scan are shown in a similar format to Fig. 8. The upper panel shows a series of calibrated spectra, each extracted at the center of one VIS line (sample 32). In the lower panel the same data have been first normalized to a common brightness level at 0.55 μm and then divided by the grand average of all spectra, in order to remove the effects of optical depth and albedo variations, as well as to emphasize the radial variations in the cutoff in reflectance at short wavelengths. Labels along the top of each plot identify prominent ring boundaries, gaps, and strong density waves. The bright feature at the inner edge of the Encke Gap is an uncorrected artifact, as are the bright bands immediately exterior to the Janus 4:3 and interior to the Mimas 5:3 resonances.

The lower panel of Fig. 9 shows the same data, normalized to a common brightness level at a wavelength of 0.55 μm and then divided by the average ring spectrum. This suppresses variations in I/F due to optical depth and particle albedo vari-

ations and permits one to visualize the variations in the rings' spectrum as function of radial position. Although there are no discrete absorption features in the rings' visible spectrum, unlike the situation in the near-IR, we do see a systematic variation in the steepness of the dropoff in reflectance shortward of ~0.6 μm. This *blue slope* (which is actually red in color) is most pronounced in the central A ring, where it appears as a dark band at the lower edge of the figure, and weaker in the innermost A ring and beyond the Encke Gap. It is weakest in the Cassini Division and in the trans-Keeler region, where it appears as a bright band in Fig. 9.

We will return to the subject of spectral variations across the rings and their possible interpretation in Section 7.

6. Ring structure and radial I/F profiles

In this section we examine the VIMS radial I/F profiles of the rings in more detail, drawing comparisons between the VIMS data and optical depth and brightness profiles obtained from Voyager observations. We also present a simple radiative transfer model for the observed I/F profiles based on the assumption of single-scattering in a classical, many-particle-thick layer. The reader interested primarily in the spectral results may wish to skip ahead to Section 7.

6.1. Comparisons with Voyager

First we compare the radial I/F profiles obtained from the Cassini VIMS data with brightness profiles obtained from Voyager images taken in 1980 and 1981 (Smith et al., 1981, 1982)—recently made available via the NASA Planetary Data System (Showalter and Gordon, 2004)—and with optical depth profiles extracted from Voyager radio and stellar occultation data (Tyler et al., 1983; Lane et al., 1982; Esposito et al., 1983a). Such comparisons should reveal any gross changes in ring structure over the past 24 years, but must be made with care because of the differences in viewing geometry among the various data sets. As noted above, at SOI the rings were seen in diffuse transmission. At low to moderate phase angles, sunlight reflected or transmitted by Saturn's rings is dominated by scattering from single ring particles[4] (Cuzzi et al., 2002, 1984; Dones et al., 1993). Analytic expressions for single-scattering by a vertically-extended layer of finite optical depth are given by Chandrasekhar (1960). For reflected light, we have

$$I/F = \frac{1}{4}\varpi_0 P(\alpha)\frac{\mu_0}{\mu_0+\mu}\left[1-e^{-\tau/\mu_{\rm eff}}\right], \tag{1}$$

where

$$\mu_{\rm eff} = \left(\mu^{-1}+\mu_0^{-1}\right)^{-1} = \frac{\mu\mu_0}{\mu+\mu_0}, \tag{2}$$

while for diffuse transmission,

$$I/F = \frac{1}{4}\varpi_0 P(\alpha)\frac{\mu_0}{\mu_0-\mu}\left[e^{-\tau/\mu_0}-e^{-\tau/\mu}\right]. \tag{3}$$

In these expressions, ϖ_0 and $P(\alpha)$ are the average single-scattering albedo and phase function of a ring particle, τ is the normal optical depth, $\mu_0 = |\cos i|$ and $\mu = |\cos e|$. The incidence (i) and emission (e) angles are measured from the northward normal to the ring plane, so that the ring opening angle, $B = 90^\circ - e$.

Although the above "classical" expressions, which assume that ring particles are well separated and thus neglect shadowing, have been shown to provide a good description of light scattered by the more optically thin regions of the rings (Cooke, 1991; Cuzzi et al., 2002), they are less successful in predicting the behavior of the more opaque A and B rings. Monte Carlo simulations of light scattering in densely packed rings provide better fits to photometric data for the B ring (Salo and Karjalainen, 2003), but do not lend themselves to simple analytic approximations. Fortunately, the SOI observations discussed here skip over the denser parts of the B ring, where we might expect Eq. (3) to fail completely.

Under the conditions of diffuse transmission which prevailed at SOI, the I/F of the rings first increases with optical depth up to a maximum at

$$\tau_{\rm max} = \frac{\mu\mu_0}{\mu-\mu_0}\ln\left(\frac{\mu}{\mu_0}\right) \simeq 2\mu_{\rm eff}, \tag{4}$$

before declining asymptotically to zero at large values of τ. The solar incidence angle, $i = 114^\circ$ for both scans, while $e = 47^\circ$ for scan 1 and $e = 63^\circ$ for scan 2, implying values for $\tau_{\rm max}$ of 0.52 and 0.43, respectively. Based on Eqs. (1) and (3), the predicted variations of reflected and diffusely-transmitted brightness with optical depth for the geometry of both Cassini SOI scans are illustrated in Fig. 10, together with the corresponding curves for the two complete Voyager imaging mosaics (Showalter and Gordon, 2004).

In the C ring and Cassini Division, where typical normal optical depths are in the range $0.05 < \tau < 0.4$, the SOI data fall in the regime of 'normal' contrast (i.e., larger τ implies larger I/F), whereas in the B ring, where $0.8 < \tau < 2.5$, we are in the regime of 'reverse' contrast (i.e., larger τ implies smaller I/F). This was already seen in Fig. 5 at the boundary between the C and B rings, where an abrupt increase in optical depth results in a sudden *decrease* in I/F and in Fig. 6, where a similar transition occurs between the Cassini Division and the A ring. For much of the A ring, except for the innermost 3000 km, $\tau \simeq 0.5$ and we are in an intermediate regime where the I/F is expected to be almost independent of optical depth.

The highest resolution Voyager 1 imaging observations were also made in diffuse transmission, but at more grazing incidence ($i = 86^\circ$) and viewing ($e = 102^\circ$) geometries. As a result, the peak I/F in this dataset occurs at $\tau_{\rm max} = 0.10$, and even the C ring plateaux with $\tau \simeq 0.4$ are seen in reverse contrast. The highest resolution Voyager 2 ring observations, on the other hand, were made in reflected light with $i = 82^\circ$ and $e = 67^\circ$. These data thus show all ring features in normal contrast, al-

[4] We adopt here the conventional terminology of 'ring particle' as referring to the orbiting bodies, typically cm to meters in size, which make up the visible rings. These ring particles are, in all likelihood, covered by a regolith of much smaller icy grains. Even at phase angles where interparticle scattering is negligible, the scattering from each particle is likely to involve multiple-scattering within this regolith.

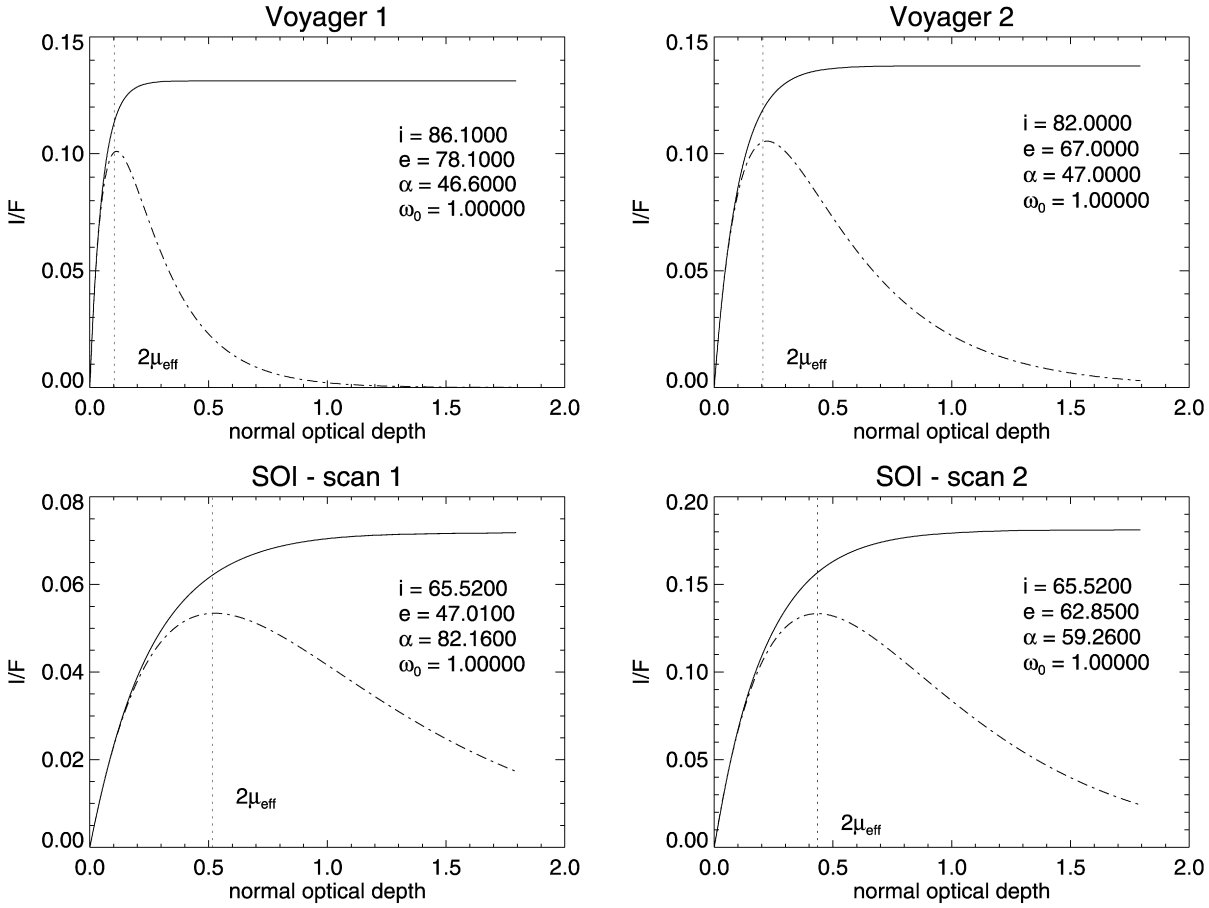

Fig. 10. Predicted variation of I/F with normal optical depth due to single-scattering calculated for the geometries relevant to the Voyager 1 and 2 imaging mosaics (Showalter and Gordon, 2004) and to the first and second VIMS SOI scans. In each panel, the solid line indicates the ring brightness in reflected light, while the dot–dashed line shows the brightness in diffusely-transmitted light for the specified incidence (i), emission (e) and phase angles (α). The Voyager 2 images were taken in reflected light; the other three datasets were taken in diffuse transmission. A vertical dotted line at $\tau_{\max} \simeq 2\mu_{\rm eff}$ indicates the optical depth at which the transmitted I/F peaks. We use the Callisto phase function of Dones et al. (1993) but assume here, for simplicity, that the single-scattering albedo, $\varpi_0 = 1.0$.

though the contrast is strongly suppressed for $\tau > 2\mu_{\rm eff} \simeq 0.2$ due to the grazing incidence angle (cf. Fig. 10).

Based on the above considerations, in Figs. 11, 12 and 15 we compare the Cassini VIMS data for the C ring and Cassini Division (where the optical depth is low and the contrast is normal) with the Voyager 2 reflected-light profile, while in Figs. 13 and 14 we compare the VIMS data for the optically thicker B ring (where the contrast is reversed) with the Voyager 1 transmitted-light profile. In each of Figs. 11–19 a common format is used. The upper panel shows the Cassini VIMS I/F profile at 1.08 μm from Fig. 5 or Fig. 6 and the Voyager 1 and/or Voyager 2 I/F profiles (Showalter and Gordon, 2004). The lower panel shows the normal optical depth profile derived from either the Voyager 1 radio (RSS) occultation data at 3.6 cm wavelength (Tyler et al., 1983; Marouf et al., 1986) or the Voyager 2 photopolarimeter (PPS) stellar occultation data at 0.27 μm (Lane et al., 1982; Esposito et al., 1983a), based on files provided by the PDS Rings Node (Showalter et al., 1996). In regions of lower optical depth such as the C ring and Cassini Division, we have chosen the radio occultation data because of their higher signal-to-noise ratio, but in most of the A and B rings the RSS data are saturated and we use the PPS data instead.

6.1.1. *Outer C ring*

Allowing for the differing incidence, emission and phase angles, we find an excellent correlation between the VIMS data and the Voyager 2 reflected light profile for the C ring in Figs. 11 and 12. We see this even for the smallest-scale (∼20 km) features resolvable in the SOI data, such as those near 86,750 and 88,800 km. These figures also demonstrate a positive correlation between the VIMS I/F profile and the Voyager RSS optical depth profile, as anticipated for regions where $\tau < \tau_{\max}$. Only in the Maxwell ringlet and perhaps in the narrow ringlet at 1.495 $R_{\rm S}$ does $\tau_{\rm RSS}$ in this region approach or exceed $\tau_{\max} = 0.52$.

The eccentric Maxwell ringlet is seen near periapse in the SOI scan, where its width is at a minimum (40 km) and its optical depth is likely to be ∼1.5 (Esposito et al., 1983b; Porco et al., 1984a); as a result it appears much darker than the nearby plateaux.

Across the ramp in optical depth that terminates the outer C ring the ratio of Cassini VIMS to Voyager 2 reflected light begins to increase. This effect is probably due, at least in part, to the optical depth approaching ∼0.20 and the resulting near-saturation of the Voyager 2 reflected-light brightness (cf. Fig. 10).

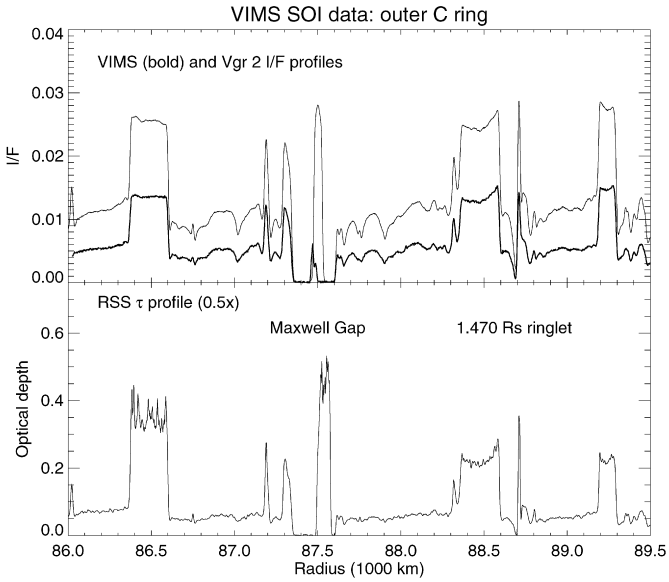

Fig. 11. In the upper panel we compare the radial I/F profile for the outer C ring at 1.08 μm derived from the first VIMS SOI scan (heavy line) with the Voyager 2 imaging profile taken in reflected light (thin line), scaled by a factor of 0.8. The lower panel shows the profile of normal optical depth from the Voyager 1 radio occultation at a wavelength of 3.6 cm, smoothed to a resolution of 20 km and scaled by a factor of 0.5 to allow for the absence of diffracted signal in the RSS data (Tyler et al., 1983). Note the eccentric and variable-width ringlet within the Maxwell Gap, and the narrow ringlet and gap at 1.470 R_S.

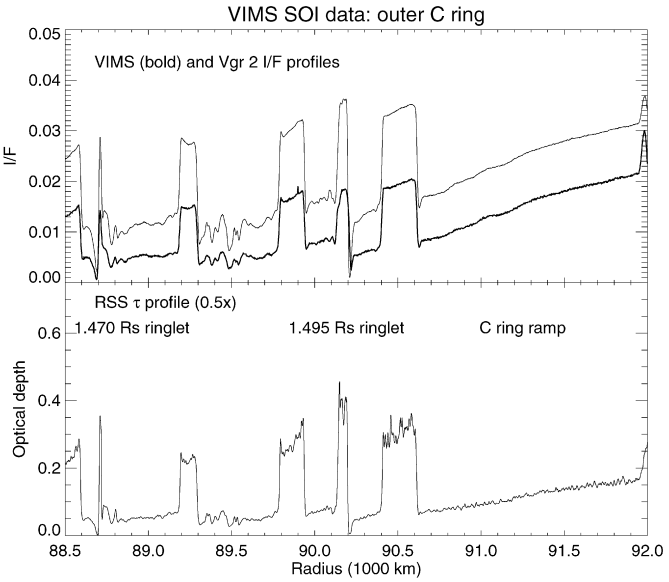

Fig. 12. In the upper panel we compare the radial I/F profile for the outermost C ring at 1.08 μm derived from the first VIMS SOI scan (heavy line) with the Voyager 2 imaging profile taken in reflected light (thin line), scaled by a factor of 0.8. The lower panel shows the profile of normal optical depth from the Voyager 1 radio occultation at a wavelength of 3.6 cm, smoothed to a resolution of 20 km and scaled by a factor of 0.5 to allow for the absence of diffracted signal in the RSS data (Tyler et al., 1983). Note the narrow ringlets and gaps at 1.470 R_S and 1.495 R_S.

6.1.2. Inner B ring

In the inner B ring we switch to the optical depth profile from the Voyager PPS occultation as our benchmark for comparison with the Cassini VIMS data in Figs. 13 and 14. The optical depths exceed 0.7 throughout this region—well above τ_{max}—resulting in a striking reversal of feature contrasts in the VIMS and Voyager 1 I/F profiles with respect to τ_{PPS}. Note that each minimum in optical depth corresponds to a peak in transmitted I/F.

As anticipated, there is generally good agreement between the VIMS I/F profile in the relatively-opaque B ring and the Voyager 1 transmitted-light profile, except in the most opaque region interior to 92,700 km. The close match of the bursts of quasi-periodic structure centered near 93,800, 95,700 and 97,500 km is especially striking. The origin of this structure is unknown, although many hypotheses have been advanced since it was first seen in Voyager images in 1981 and later characterized by Horn and Cuzzi (1996). Several authors have proposed some form of radial instability or overstability (Ward, 1981; Lin and Bodenheimer, 1981; Lukkari, 1981; Borderies et al., 1985; Goertz and Morfill, 1988; Schmit and Tscharnuter, 1999), while Durisen et al. (1989) and Durisen (1995) invoked ballistic transport processes. More recently, Tremaine (2003) has suggested that temporary 'crystallization' can take place in the B ring. From Fig. 13 it is clear that not only is this wavelike structure probably axisymmetric (i.e., it is not a tightly wrapped spiral like a density wave or a moonlet wake) but that it has remained unchanged in amplitude and phase over 24 years.

Some small differences are seen between the Voyager 1 and VIMS transmitted-light profiles, most notably the small dips at 94,480 and 95,210 km at either end of the prominent 'flat spot.' Differences also occur in the neighborhood of the strong Janus 2:1 density wave, but these are likely due to intrinsic longitudinal and/or temporal variations in the wave profile (Tiscareno et al., 2006b).

6.1.3. Cassini Division

Optical depths in the Cassini Division are comparable to those in the C ring, and in Fig. 15 we compare the Cassini VIMS data with the Voyager RSS optical depth profile and the Voyager 2 reflected-light profile, as we did for the C ring above. Again we see a strong positive correlation between the VIMS I/F profile and τ_{RSS}, as well as between the VIMS and Voyager 2 I/F profiles. The only significant deviations are associated with the non-circular outer edge of the B ring at ∼117,600 km (Porco et al., 1984b) and the eccentric Huygens ringlet at 117,820 km (Turtle et al., 1991). The latter appears rather dim in the VIMS data, either because it is unresolved at our resolution of ∼30 km, or more probably because its optical depth significantly exceeds $\tau_{max} \simeq 0.43$.

An interesting intermediate case is provided by the narrow ringlet at 120,070 km within the Outer rift and the broad, triple-peaked band centered at 120,700 km. The latter's internal structure is quite muted in both I/F profiles, but for different reasons: the VIMS transmitted-light profile is flat because the average optical depth here approaches τ_{max}, while the Voyager 2 reflected light profile is nearing its saturation level for $\tau \gg 2\mu_{eff} \simeq 0.2$ (cf. Fig. 10).

As in the case of the C ring ramp, the ratio of Cassini VIMS to Voyager 2 I/F steadily increases across the ramp that ter-

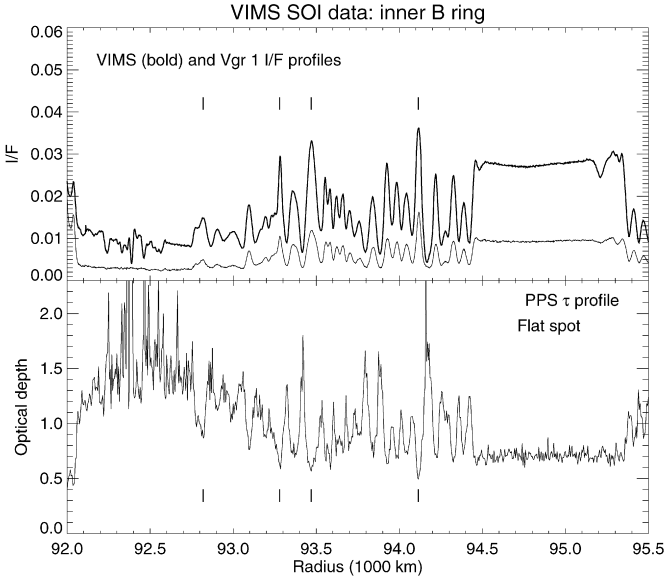

Fig. 13. In the upper panel we compare the radial I/F profile for the innermost B ring at 1.08 μm derived from the first VIMS SOI scan (heavy line) with the Voyager 1 imaging profile (thin line) taken in transmitted light, scaled by a factor of 1.5. The lower panel shows the profile of normal optical depth from the Voyager 2 PPS stellar occultation at 0.27 μm, smoothed to a resolution of 20 km. Note the reversal of contrast in both transmitted light profiles, with the less opaque regions, denoted by tick marks, appearing brighter.

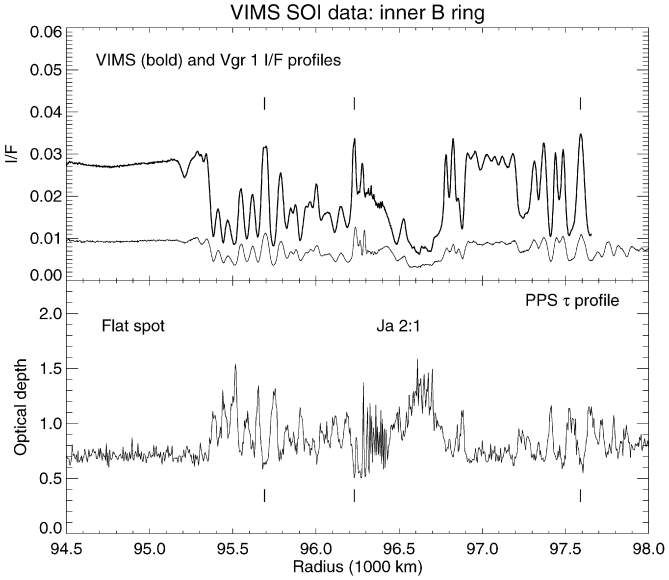

Fig. 14. In the upper panel we compare the radial I/F profile for the inner B ring at 1.08 μm derived from the first VIMS SOI scan (heavy line) with the Voyager 1 imaging profile (thin line) taken in transmitted light, scaled by a factor of 1.5. The lower panel shows the profile of normal optical depth from the Voyager 2 PPS stellar occultation at 0.27 μm, smoothed to a resolution of 20 km. Note again the reversal of contrast in both transmitted light profiles. The oscillatory structure near 96,500 km due to the Janus 2:1 density wave is not well resolved.

minates the Cassini Division, although in this case the optical depth barely reaches 0.15 at the outer edge and saturation of the Voyager data seems less likely to be responsible.

6.1.4. A ring

As in the B ring, the RSS optical depths are largely saturated in the A ring and we switch back to the Voyager PPS optical depth profile as our benchmark for comparisons with the VIMS data in Figs. 16–19. As we cross from the Cassini Division ramp into the inner A ring at 122,000 km, the optical depth increases at first to ∼0.6 and then to ∼1.0, well above $\tau_{\max} = 0.43$. The VIMS I/F shows a brief peak (as it does at the inner edge of the B ring in Fig. 5) and then rapidly decreases to a value similar to that of the inner Cassini Division.

A potential complication in comparing A ring scans made at different longitudes and viewing geometries is the A ring's well-known azimuthal brightness asymmetry (Thompson et al., 1981; Dones et al., 1993; French et al., 2006), which is generally attributed to self-gravity wakes driven by a combination of Keplerian shear and mutual gravitational interactions between the ring particles (Colombo et al., 1976; Salo, 1995). Associated with the wakes are significant azimuthal variations in the line-of-sight optical depth of the rings (Salo et al., 2004; Colwell et al., 2006; Hedman et al., 2007), although these are unlikely to have a large effect on the SOI data due to the relatively steep incidence and emission angles (cf. Fig. 10).

Interior to ∼126,000 km, τ exceeds $\tau_{\max}$ and the agreement with the Voyager 1 transmitted-light profile in Fig. 16 is quite good, as it is for the inner B ring, both in terms of overall shape and in small-scale structure. Small differences do occur, such as the dip at 124,700 km, which is more prominent in the VIMS data, and that at 125,750 km, which is only seen clearly in the Voyager 1 data. As expected, there is a strong anti-correlation with $\tau_{\rm PPS}$ here, with the maxima in optical depth coinciding with minima in transmitted I/F.

Outside a radius of ∼126,000 km, $\tau_{\rm PPS}$ is close to $\tau_{\max}$ and we expect this region to show relatively little contrast in I/F in the SOI data (cf. Fig. 10), as confirmed by Figs. 17 and 18. In the middle A ring (126,000–133,000 km), the overall shapes of the Voyager 1 and VIMS I/F profiles are similar, but a gradual increase in the Voyager I/F with radius reflects the slow decrease in $\tau_{\rm PPS}$ out to ∼130,000 km, coupled with the fact that $\tau > \tau_{\max}$ for the Voyager 1 data set.

Each of the strong density waves in the A ring driven by the Janus 4:3, 5:4 and 6:5 inner Lindblad resonances and the Mimas 5:3 ILR, as well as the bending wave driven by the Mimas 5:3 inner vertical resonance, appears as a local minimum in transmitted I/F, consistent with their enhanced average optical depths in the PPS profile. However, several of the weaker Prometheus and Pandora density waves—indicated by tick marks in the figures—appear *fainter* in the Voyager 1 profile but *brighter* than their immediate surroundings in the VIMS data.

Very prominent in the Cassini SOI data—though they also appear in the Voyager I/F profiles—are broad "halos" of enhanced I/F which extend ∼700 km on either side of three of the four strong density waves in the A ring: those associated with the Janus 4:3 and 5:4 and Mimas 5:3 ILRs. However, in the Voyager 1 transmitted-light profile, the halos appear as *minima* in I/F relative to the nearby A ring (including the Janus 6:5 density wave in Fig. 19 but not the Janus 4:3 wave). In reflected

light the halos appear as brightness *maxima* at phase angles below 30° and as *minima* at phase angles of 50–70° (cf. Figs. 7 and 8 in Dones et al., 1993). In the Voyager 2 reflected-light profile in Fig. 18—obtained at a phase angle of 47°—the halos are not prominent, but appear as slight increases in I/F relative to their surroundings.

The halos also appear as zones of slightly enhanced optical depth in the 28 Sgr occultation data (see Nicholson et al., 2000, Fig. 14), but seem to have little expression in the somewhat noisier PPS data. Although a small increase in optical depth in the halos could account for either a higher or lower I/F in transmitted light, depending on the local value of τ, this is un-

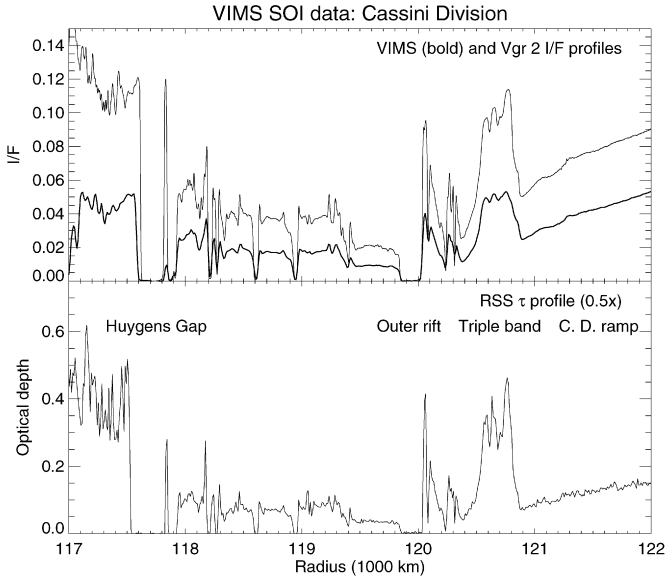

Fig. 15. In the upper panel we compare the radial I/F profile for the Cassini Division at 1.08 μm derived from the second VIMS SOI scan (heavy line) with the Voyager 2 imaging profile taken in reflected light (thin line), scaled by a factor of 2.0. The lower panel shows the profile of normal optical depth from the Voyager 1 radio occultation at a wavelength of 3.6 cm, smoothed to a resolution of 20 km and scaled by a factor of 0.5 to allow for the absence of diffracted signal in the RSS data (Tyler et al., 1983). Note the narrow, eccentric Huygens ringlet which inhabits the eponymous gap, as well as the similar ringlet in the Outer rift and the unique triple-peaked band at ∼120,700 km.

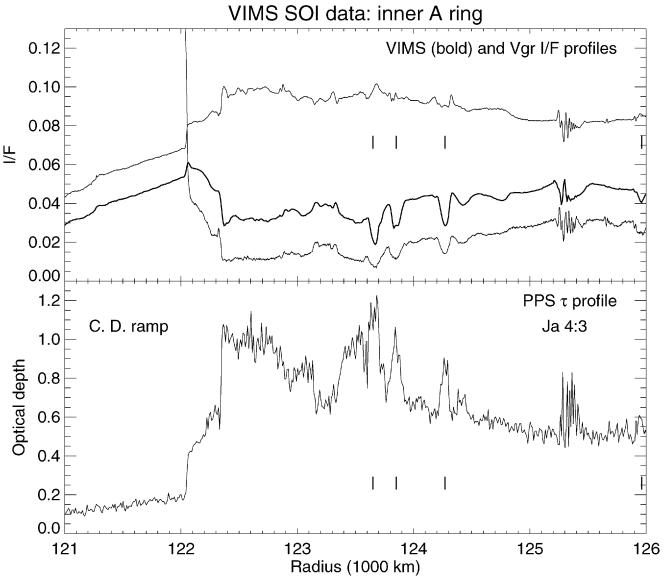

Fig. 16. In the upper panel we compare the radial I/F profile for the inner A ring at 1.08 μm derived from the second VIMS SOI scan (heavy line) with the Voyager 1 imaging profile (lower curve) taken in transmitted light, scaled by a factor of 3.5, and the Voyager 2 imaging profile (upper curve) taken in reflected light, scaled by a factor of 1.5. The lower panel shows the profile of normal optical depth from the Voyager 2 PPS stellar occultation at 0.27 μm, smoothed to a resolution of 20 km. Note the reversal of contrast between the transmitted and reflected light profiles, with more opaque regions appearing fainter in the former and generally brighter in the latter.

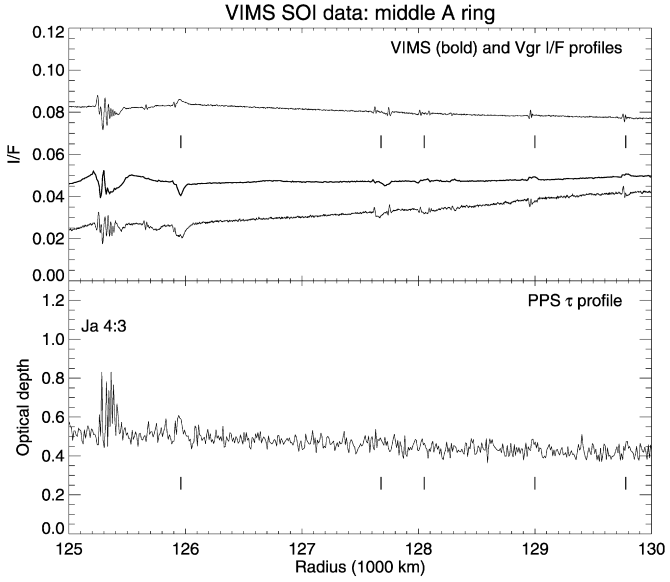

Fig. 17. In the upper panel we compare the radial I/F profile for the middle A ring at 1.08 μm derived from the second VIMS SOI scan (heavy line) with the Voyager 1 imaging profile (lower curve) taken in transmitted light, scaled by a factor of 3.0, and the Voyager 2 imaging profile (upper curve) taken in reflected light, scaled by a factor of 1.5. The lower panel shows the profile of normal optical depth from the Voyager 2 PPS stellar occultation at 0.27 μm, smoothed to a resolution of 20 km. Note the strong Janus 4:3 density wave as well as several weaker, unresolved waves due to Pandora and Prometheus, denoted by tick marks.

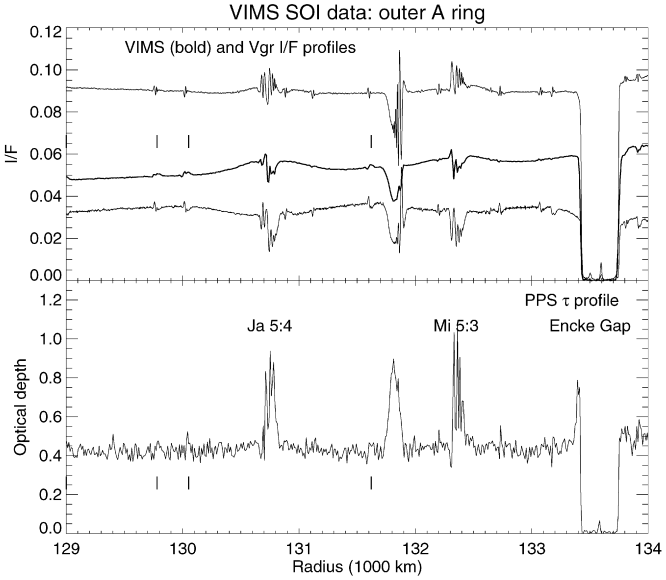

Fig. 18. In the upper panel we compare the radial I/F profile for the outer A ring at 1.08 μm derived from the second VIMS SOI scan (heavy line) with the Voyager 1 imaging profile (lower curve) taken in transmitted light, scaled by a factor of 2.5, and the Voyager 2 imaging profile (upper curve) taken in reflected light, scaled by a factor of 1.75. The lower panel shows the profile of normal optical depth from the Voyager 2 PPS stellar occultation at 0.27 μm, smoothed to a resolution of 20 km. Note the variable appearance of the halos which surround the strong Janus 5:4 and Mimas 5:3 density waves in different lighting geometries, and the absence of any similar halo around the Mimas 5:3 bending wave at 131,800 km. Tick marks denote unresolved density waves due to Pandora and Prometheus.

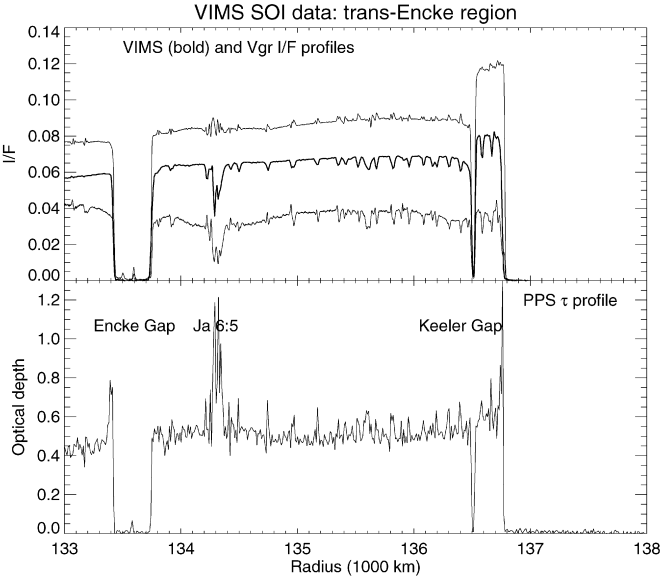

Fig. 19. In the upper panel we compare the radial I/F profile for the trans-Encke region of the A ring at 1.08 μm derived from the second VIMS SOI scan (heavy line) with the Voyager 1 imaging profile (lower curve) taken in transmitted light, scaled by a factor of 3.0, and the Voyager 2 imaging profile (upper curve) taken in reflected light, scaled by a factor of 1.5. The lower panel shows the profile of normal optical depth from the Voyager 2 PPS stellar occultation at 0.27 μm, smoothed to a resolution of 20 km. Note the contrast reversal of the many weak density waves in this region between transmitted and reflected light profiles, as well as the unusual brightness of the trans-Keeler region in the Voyager 2 profile. The halo around the Janus 6:5 density wave is much less-pronounced than those in Fig. 18. With an average width of 35 km, the Keeler Gap is only just resolved in the VIMS SOI data.

likely to account for what is seen in the VIMS SOI data where the average optical depth is quite close to $\tau_{\max}$. An alternative explanation is suggested by the photometric analysis of Dones et al. (1993), who report that the halos are characterized by a more strongly-backscattering phase function than applies to the average A ring (see their Fig. 14). This in turn, they argue, is consistent with the rings' vertical structure being closer to a monolayer in these regions than in their surroundings.

Significantly, the Mimas 5:3 bending wave shows no halo either in I/F (Fig. 18) or in optical depth, suggesting that halos may be connected with the enhanced collisional environment thought to be associated with strongly nonlinear density waves.[5] Although their nature is currently mysterious, the halos also show a distinct spectral signature, which we discuss in Section 7.2 below.

Beyond the Encke gap, the shape of the VIMS I/F profile in Fig. 19 more closely resembles that of the Voyager 2 reflected-light profile, although neither conforms to the PPS optical depth profile. In the VIMS profile the I/F reaches a broad maximum at ∼136,000 km, just interior to the Keeler Gap, before increasing abruptly outside the gap by ∼20%. There is only a modest increase in τ_{PPS} in this region, so this is unlikely to be the cause of the observed brightening. We also see a marked change in the near-infrared spectrum in this outermost zone of the A ring, as discussed in Section 7.2 below.

Dones et al. (1993) find significant differences between the photometric behavior of the trans-Encke region and the remainder of the A ring, and even larger differences in the trans-Keeler region. Beyond the Encke Gap, the particle phase function is somewhat less backscattering, suggesting a physically-thicker ring. Outside the Keeler Gap, this trend is amplified, while at the same time the particle single-scattering albedo inferred by Dones et al., increases by ∼20%, matching the increase in I/F we see in this region. Estrada and Cuzzi (1996) also report a significant difference in the visible color of the trans-Keeler region as compared with the rest of the A ring, suggesting that it be referred to as the "Keeler ringlet."

The small-scale structure in the trans-Encke region is mostly due to a plethora of unresolved Prometheus and Pandora density waves, all of which appear noticeably *dimmer* than their surroundings in the VIMS data, unlike their cousins interior to the Encke Gap which generally appear *brighter* than the background. The reason for this behavior is unknown, but it may involve subtle variations in $\tau_{\max}$ associated with the ring's increased vertical thickness as we move outwards (cf. paragraph above).

6.2. Single-scattering models

Previous investigations of the photometric behavior of the A, B and C rings at visual wavelengths have shown that individual

[5] Bending waves involve vertical displacements out of the mean ring plane, rather than the oscillations in ring particle surface density in density waves, and are thus not expected to lead to significantly enhanced particle collision rates.

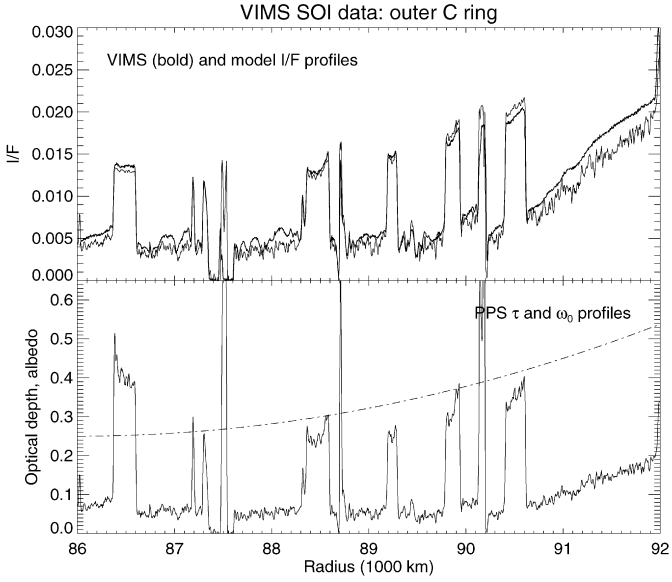

Fig. 20. In the upper panel we compare the radial I/F profile for the outer C ring at 1.08 μm derived from the first VIMS SOI scan (smooth, heavy line) with a theoretical single-scattering model (noisier, thin line). The model was calculated from Eq. (3), using the PPS optical depth profile and the profile of single-scattering albedo (dot–dashed line) from Cooke (1991), as shown in the lower panel.

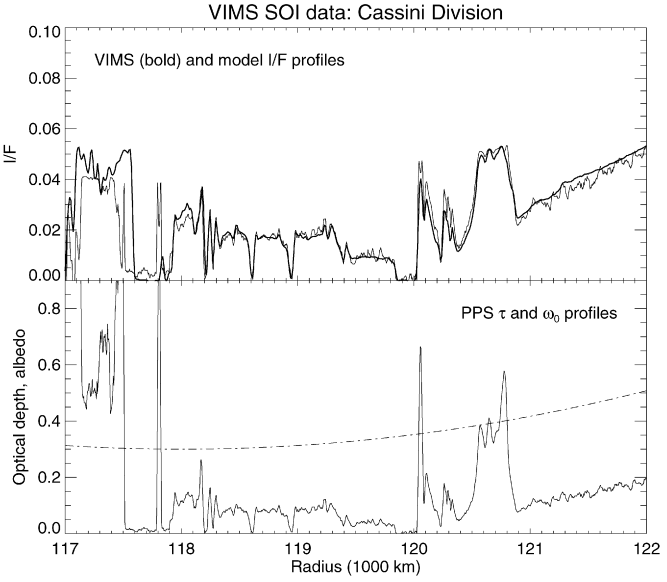

Fig. 21. In the upper panel we compare the radial I/F profile for the Cassini Division at 1.08 μm derived from the second VIMS SOI scan (smooth, heavy line) with a theoretical single-scattering model (noisier, thin line). The model was calculated from Eq. (3), using the PPS optical depth profile and a simple quadratic expression for the single-scattering albedo (dot–dashed line; see text), as shown in the lower panel.

ring particles are strongly backscattering, with a phase function similar to that of the icy Galilean satellites (Dones et al., 1993; Doyle et al., 1989; Cooke, 1991). A consequence of this is that light scattered by the rings at low to moderate phase angles is dominated by single-scattering (Cuzzi et al., 1984), with interparticle scattering becoming important only at high phase angles and in regions where the optical depth, $\tau \geqslant 1$ (Cuzzi et al., 2002). In an analysis of Voyager images of the C ring, where τ rarely exceeds 0.4, Cooke (1991) found that a classical single-scattering model based on the analytic expressions in Eqs. (1) and (3) above provides a good quantitative fit to the observed I/F for images taken at a wide variety of viewing geometries including both reflection and diffuse transmission. Analysis of the variation in ring brightness with opening angle in HST images taken at wavelengths of 0.336 and 0.555 μm led Cuzzi et al. (2002) to conclude that the Cassini Division and the innermost part of the B ring, as well as the C ring and much of the A ring, are also well described by such a classical model.

Cuzzi et al., argued further that although the well-known increase of I/F with opening angle for the middle B ring is incompatible with single-scattering in a classical, many-particle-thick ring, interparticle scattering is not the answer, and is in fact unimportant at low phase angles. (The steep increase in particle albedo between 0.336 and 0.555 μm would lead to an even steeper increase in multiply-scattered light at the longer wavelength, contrary to the HST observations.) Salo and Karjalainen (2003) have suggested that this so-called 'tilt effect' may instead reflect vertical stratification in the B ring, with the largest and brightest particles being confined to a thin central layer, surrounded by a halo of smaller and darker particles. The former become increasingly visible at large opening angles, increasing the overall I/F even as the ring becomes less opaque. Such a model may also provide an explanation for the otherwise puzzling increase in the rings' radar circular polarization ratio with opening angle (Nicholson et al., 2005).

We were thus led to investigate the degree to which the near-infrared radial profiles of I/F in Figs. 5 and 6 could be modeled in terms of single-scattering by a "classical" many-particle-thick layer. Our photometric model is the same as that used by Cooke (1991) and Cuzzi et al. (2002), with the diffusely transmitted I/F given by Eq. (3) above and illustrated in Fig. 10. Appropriate values of i, e and α are given for each SOI scan in Table 1. For $\tau(r)$ we use the Voyager PPS occultation profile, and for $P(\alpha)$ we use the analytic approximation to Callisto's phase function introduced by Dones et al.:

$$P(\alpha) = c_n(\pi - \alpha)^n \tag{5}$$

with $n = 3.301$ and $c_n = 0.130$. The only free parameter in the model is the single-scattering albedo at 1.08 μm, ϖ_0.

Model fits for the VIMS profiles of the outer C ring and the Cassini Division are shown in Figs. 20 and 21, respectively. Because of their relatively low optical depths, these two regions are expected to provide the best match to a single-scattering model, and indeed this is so. For the C ring we have used a simple polynomial approximation to the results of Cooke (1991):

$$\varpi_0 = 0.25 + 8.0 \times 10^{-9}(r - r_0)^2, \tag{6}$$

where $r_0 = 86{,}000$ km. This model was derived from images taken with the Voyager clear filter ($\lambda_{\rm eff} = 0.45$ μm), and is shown as the dot–dashed curve in Fig. 20. Note that the single-scattering model accurately predicts the relative brightness of plateau and background regions in the C ring, as well as the increasing I/F of the four plateaux between 88,500 and 90,500 km. Across the outer ramp, the I/F is underestimated

by ∼10%, suggesting either that ϖ_0 increases slightly more rapidly with radius at 1.08 μm than given by Eq. (6) or that interparticle scattering is beginning to become significant as $\tau_{\rm PPS}$ and ϖ_0 increase.

Our initial model for the Cassini Division used a constant value of $\varpi_0 = 0.32$, as reported by Smith et al. (1981), again for the Voyager clear filter. This provides an excellent fit to the VIMS data for radii $r \leqslant 120{,}500$ km, but underestimates the observed I/F by ∼15% in the triple-peaked feature and by up to 30% in the ramp. An improved and quite satisfactory model shown in Fig. 21 uses a polynomial expression for ϖ_0 similar to that used in the outer C ring:

$$\varpi_0 = 0.30 + 1.3 \times 10^{-8}(r - r_0)^2 \tag{7}$$

with $r_0 = 118{,}000$ km. This expression is also consistent with the results of Dones et al. (1993), who found that ϖ_0 increases from ∼0.40 to 0.45 across the outer Cassini Division.

In the inner B ring, where $0.7 \leqslant \tau \leqslant 1.5$, the single-scattering model provides a quantitatively less-satisfactory fit, but still succeeds qualitatively in reproducing the main features in the SOI profile, including the reverse contrast of the oscillatory structure noted in Figs. 13 and 14. The model in Fig. 22 uses a constant $\varpi_0 = 0.55$, as derived by Doyle et al. (1989) from Voyager clear-filter images of the B ring, which provides an excellent fit to the I/F in the two "flat spots." Although it overestimates the average I/F in the oscillatory regions, the single-scattering model does a reasonable job at predicting the amplitude of the oscillations. Cuzzi et al. (2002) also found that the variation of the lit-side I/F with opening angle in the inner B ring agreed quite well with the predictions of the classical model [i.e., with Eq. (1)], unlike the situation in the more opaque middle and outer B rings.

The single-scattering model is least successful in the A ring, even though the optical depth here is only about one-half that of the inner B ring. The model shown in Figs. 23 and 24 uses a uniform value of $\varpi_0 = 0.50$, after Dones et al. (1993), together with the standard Callisto phase function, but provides a rather poor fit to the SOI data, especially in the inner A ring. With an average optical depth of ∼0.45, much of the A ring falls near the peak of the predicted diffusely-transmitted I/F in Fig. 10, resulting in a single-scattering model profile which is essentially independent of optical depth. However, the I/F in the SOI data increases smoothly and almost monotonically from ∼0.045 at 125,000 km to a maximum of ∼0.065 at 136,000 km.

Although the absolute level of I/F in the inner A ring is seriously overestimated by Eq. (3), the model again does a reasonable job of reproducing the high-frequency structure in the SOI profile. In the outer A ring, on the other hand, the classical model actually matches the average level of the observed I/F profile reasonably well, but not its detailed shape. Beyond the Keeler Gap the VIMS SOI profile brightens abruptly by ∼20%. As noted in Section 6.1.4 above, this is consistent with a similar increase in ϖ_0 in this region inferred by Dones et al. (1993).

In their comprehensive study of A ring photometry based on Voyager imaging, Dones et al., also found a poor fit between this ring's brightness profile in reflected light and the predictions of a classical, many-particle-thick scattering model,

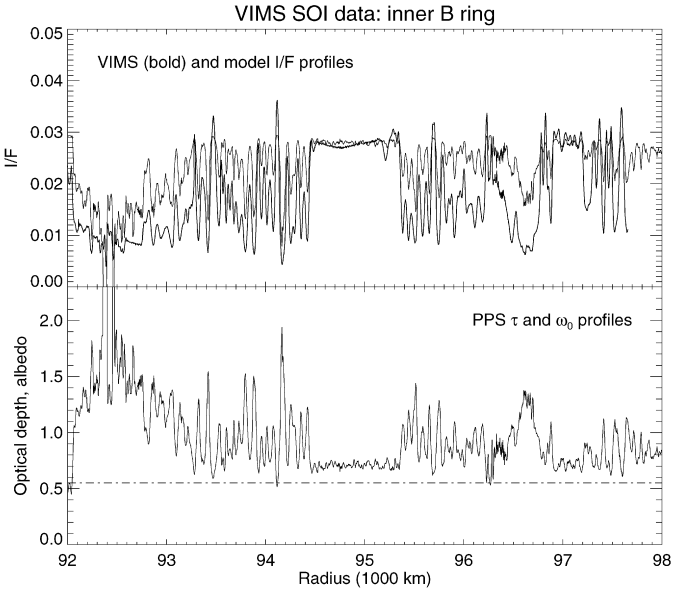

Fig. 22. In the upper panel we compare the radial I/F profile for the inner B ring at 1.08 μm derived from the first VIMS SOI scan (smooth, heavy line) with a theoretical single-scattering model (noisier, thin line). The model was calculated from Eq. (3), using the PPS optical depth profile and a constant single-scattering albedo of 0.55 (dot–dashed line) from Doyle et al. (1989), as shown in the lower panel. In this region, the single-scattering model generally overestimates the average I/F, except in the two 'flat spots' at 95,000 and 97,000 km.

subject to the assumption that the single-scattering albedo and phase function did not vary with radius (cf. their Fig. 20). From an analysis of the variation in I/F with phase angle, they concluded (i) that ϖ_0 is almost constant at radii interior to the Keeler Gap, with an average value of ∼0.50, but increases to ∼0.60 in the trans-Keeler region and (ii) that the ring particle phase function becomes gradually less backscattering as the radius increases from 126,000 to 136,000 km, and then much less backscattering in the trans-Keeler region (cf. their Fig. 14). Given the 59° phase angle of the SOI data in the A ring, a similar radial variation in phase function at 1.08 μm could result in the outward increase in I/F seen in Figs. 23 and 24. It is also quite possible that the classical single-scattering model underlying Eq. (3) breaks down in the inner A ring, as suggested by the poor fits to the phase function in this region found by Dones et al., based on this same model (cf. their Fig. 17).

As noted above, an additional complication in modelling the A ring's I/F is the strong azimuthal asymmetry seen at low ring opening angles and attributed to sub-kilometer scale self-gravity wakes. Although the asymmetry amplitude itself is predicted to be relatively small at the 27° opening angle of the SOI scan across the A ring (Salo et al., 2004), recent analyses of Cassini stellar occultation data by Colwell et al. (2006) and Hedman et al. (2007) show that much of the A ring is not a homogeneous layer but rather an alternating patchwork of opaque wakes and optically-thin interwake 'gaps.' According to this model, the diffusely-transmitted light seen at SOI emerges almost entirely from the gaps, where $0.1 < \tau < 0.25$ and a normal contrast regime is predicted by Fig. 10.

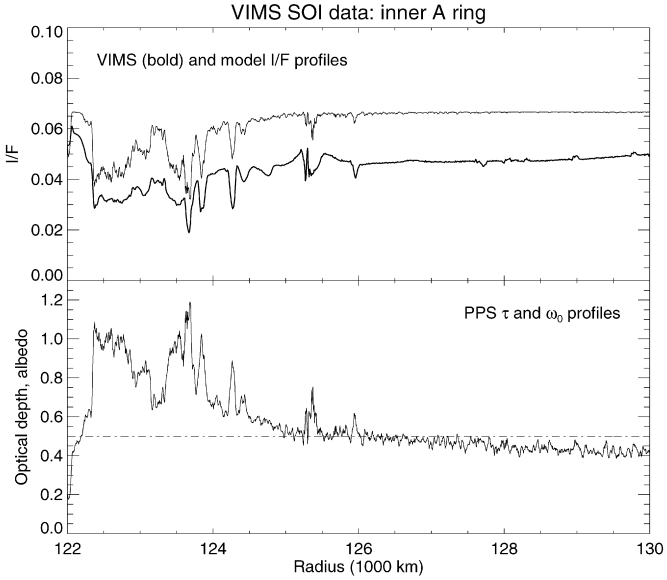

Fig. 23. In the upper panel we compare the radial I/F profile for the inner A ring at 1.08 μm derived from the second VIMS SOI scan (smooth, heavy line) with a theoretical single-scattering model (noisier, thin line). The model was calculated from Eq. (3), using the PPS optical depth profile and a constant single-scattering albedo of 0.50 (dot–dashed line) from Dones et al. (1993), as shown in the lower panel. Note the lack of contrast in the model I/F for $0.3 \leqslant \tau \leqslant 0.6$, as predicted by Fig. 10.

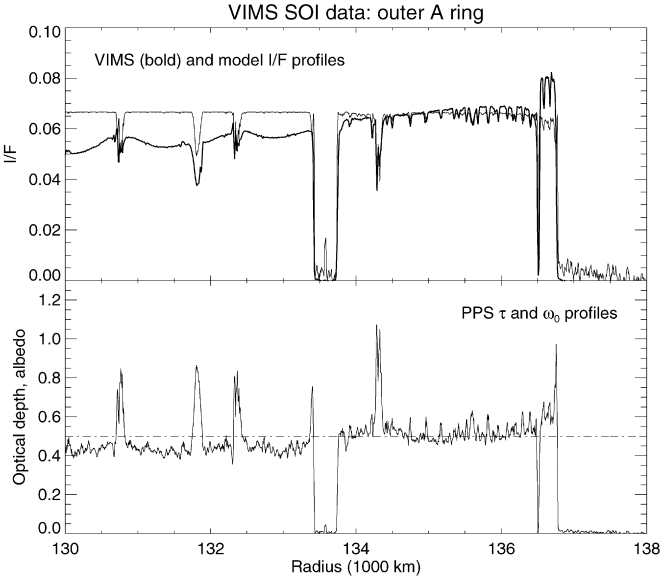

Fig. 24. In the upper panel we compare the radial I/F profile for the outer A ring at 1.08 μm derived from the second VIMS SOI scan (smooth, heavy line) with a theoretical single-scattering model (noisier, thin line). The model was calculated from Eq. (3), using the PPS optical depth profile and a constant single-scattering albedo of 0.50 (dot–dashed line) from Dones et al. (1993), as shown in the lower panel. Note the lack of contrast in the model I/F for $0.3 \leqslant \tau \leqslant 0.6$, as predicted by Fig. 10, and the anomalous reflectance of the region outside the Keeler Gap at 136,500 km.

In summary, we find that the classical, single-scattering model represented by Eq. (3) provides excellent fits to the VIMS I/F profiles for the C ring and Cassini Division, and fair agreement in the inner B ring and outer A ring. It is less successful in the inner two-thirds of the A ring, where independent photometric evidence suggests that the ring may be nearer to a monolayer in vertical structure and where self-gravity wakes are important.

In closing this discussion, we note that the VIMS profiles in Figs. 20–24 were obtained at 1.08 μm, but for our photometric models we have adopted the particle single-scattering albedos derived by Doyle et al. (1989), Cooke (1991) and Dones et al. (1993) using images taken with the Voyager clear filter at an effective wavelength of 0.45 μm. Given the very red spectrum of the A and B rings in the 0.4–1.0 μm range (Karkoschka, 1994; Cuzzi et al., 2002; Poulet et al., 2003; Fig. 3), one would expect ϖ_0 to be 25–30% greater at 1.08 μm than it is at 0.45 μm, yet we find essentially the same values. In part, this may reflect the more neutral spectra of the C ring and Cassini Division (Estrada and Cuzzi, 1996; Cuzzi et al., 2002), but this cannot be the whole story. Possible explanations include a ring particle phase function at 1.08 μm which is steeper than that adopted by Dones et al. (1993) at 0.45 μm, known deficiencies in the flux calibration of the Voyager cameras (see the discussion by Cuzzi and Estrada, 1998), or an error in the VIMS absolute flux calibration. Comparisons with HST ring data suggest that the VIMS calibration may be too low by 10–15%. Future VIMS observations of the rings to be acquired at a wide range of phase angles should resolve the phase function issue, while icy satellite observations will be used to improve the absolute calibration.

7. Ring spectral variations

In this section we explore the spectral properties of the rings as a function of radial location. We begin by comparing the IR spectra of several broad, structurally-homogeneous regions. Next we quantify several observed spectral variations by plotting radial profiles of band depths and spectral slopes at selected wavelengths. We present these data for scans 1 and 2 separately, and then discuss their similarities and differences.

7.1. Outer C ring and inner B ring (scan 1)

Fig. 25 illustrates the average IR spectra of several regions from scan 1, including the middle and outer C ring, the transitional 'ramp' at the outer edge of the C ring and the inner B ring. Both the trans-Maxwell C ring and C ring ramp show relatively weak water ice bands at 1.5 and 2.0 μm, as well as a broad but shallow absorption centered near 1.2 μm. As discussed in Section 5.1 above, the latter feature may be due to an unspecified Fe^{+2}-bearing silicate mineral, but may also be a characteristic of water ice grains at this phase angle. The ice bands are even weaker in the middle C ring, while the 'silicate feature' is masked here by a series of narrow absorptions at 1.00, 1.15 and 1.35 μm, attributed in Section 5.3 above to methane absorption in Saturn's upper atmosphere. In the inner B ring the broad 'silicate feature' disappears, while the 1.5 and 2.0 μm ice bands strengthen noticeably.

Fig. 26 shows the depths of the 1.5 and 2.0 μm ice bands as a function of radius for scan 1, along with the average I/F measured in the continuum around 1.8 μm. The band depths,

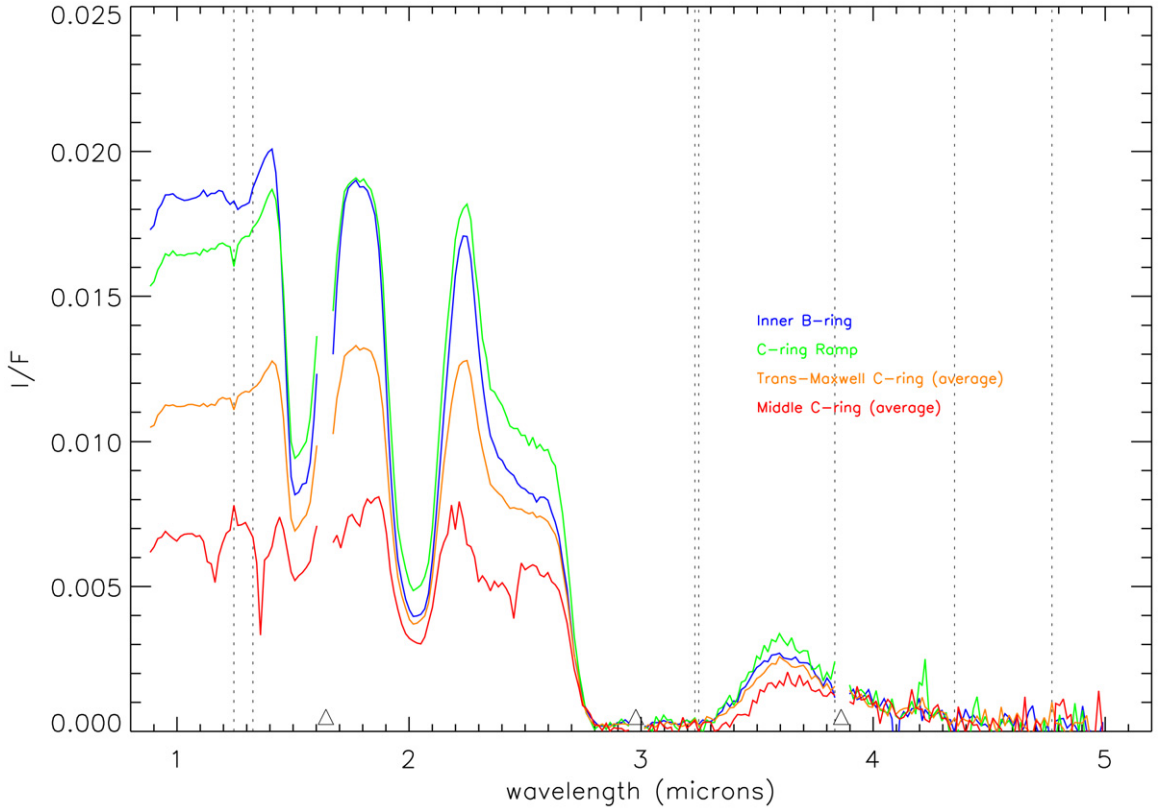

Fig. 25. Infrared spectra of the middle and outer C ring, the ramp at the outer edge of the C ring and the inner part of the B ring, all derived from the first VIMS SOI scan. Triangles indicate gaps between the IR focal plane blocking filters where the spectra may be unreliable; these channels have been suppressed. Vertical dotted lines indicate hot pixels, which can saturate in long integrations. Note the features at 1.0, 1.15, 1.35, 1.75 and 2.3 μm in the middle C ring spectrum, identified in the text with methane absorption in Saturn's stratosphere.

D_B, are computed as defined by Clark and Roush (1984):

$$D_B = \frac{I_{\text{cont}} - I_{\text{band}}}{I_{\text{cont}}}. \tag{8}$$

For the 1.5 micron band, I_{band} is the average I/F between 1.50 and 1.57 μm and I_{cont} is the average continuum I/F between 1.75 and 1.84 μm. For the 2.0 micron band, I_{band} is the average I/F between 1.98 and 2.09 μm with the same I_{cont}. Note that each of these band depths is defined so that it should always have a value between 0 and 1, and so that the *larger* the band-depth, the *deeper* the corresponding ice band(s).

In Fig. 26 we see that both ice bands grow steadily stronger across the outer C ring, including the ramp, and then stabilize in the inner B ring at a radius of about 93,000 km. These trends can probably be attributed to regional variations in ice purity and/or regolith grain size, in the sense that ring particles in the B ring are either less-contaminated with non-icy material or have larger regolith ice grain sizes than do particles in the C ring. Note in particular that there is not a sharp transition in ice band depths between the C and B rings, despite the abrupt changes in optical depth and I/F at the outer edge of the ramp. This clearly demonstrates that increases in band depth are *not* primarily due to increases in multiple scattering between ring particles, which would be expected to correlate strongly with optical depth.

Instead, the large-scale variations in band depth likely represent a gradient in the composition or regolith properties of individual particles across this region. This would be consistent with the Voyager imaging data at optical wavelengths, which indicate a similarly smooth change in color between the outer C ring and B ring (Estrada and Cuzzi, 1996). Such a compositional gradient may be the result of ballistic transport of material between the B and C rings (Cuzzi and Estrada, 1998).

Within the C ring, we observe that the ice bands in the plateaux are slightly enhanced compared to those in the nearby low-τ background, but that this enhancement is at most 10% whereas the optical depth varies by a factor of 3–4. This again implies that interparticle scattering is relatively unimportant in this particular viewing geometry. Estrada et al. (2003) also noted color differences between the plateaux and the background C ring, but only in Voyager's violet filter.

In the inner B ring, and especially within the 80-km scale oscillations between 93,000 and 96,000 km, we find that the ice bands are again slightly deeper in regions of higher I/F, which here corresponds to *lower* values of optical depth (cf. Figs. 13 and 14 above). This runs counter to our expectation that regions of higher optical depth will show more interparticle scattering and thus have deeper ice-bands, as is seen at least weakly in the C ring. Instead the anticorrelation between optical depth and ice band depth observed in this region probably arises from differences in the effective grain size or packing density within the ring particle regoliths, perhaps due to differing collisional regimes.

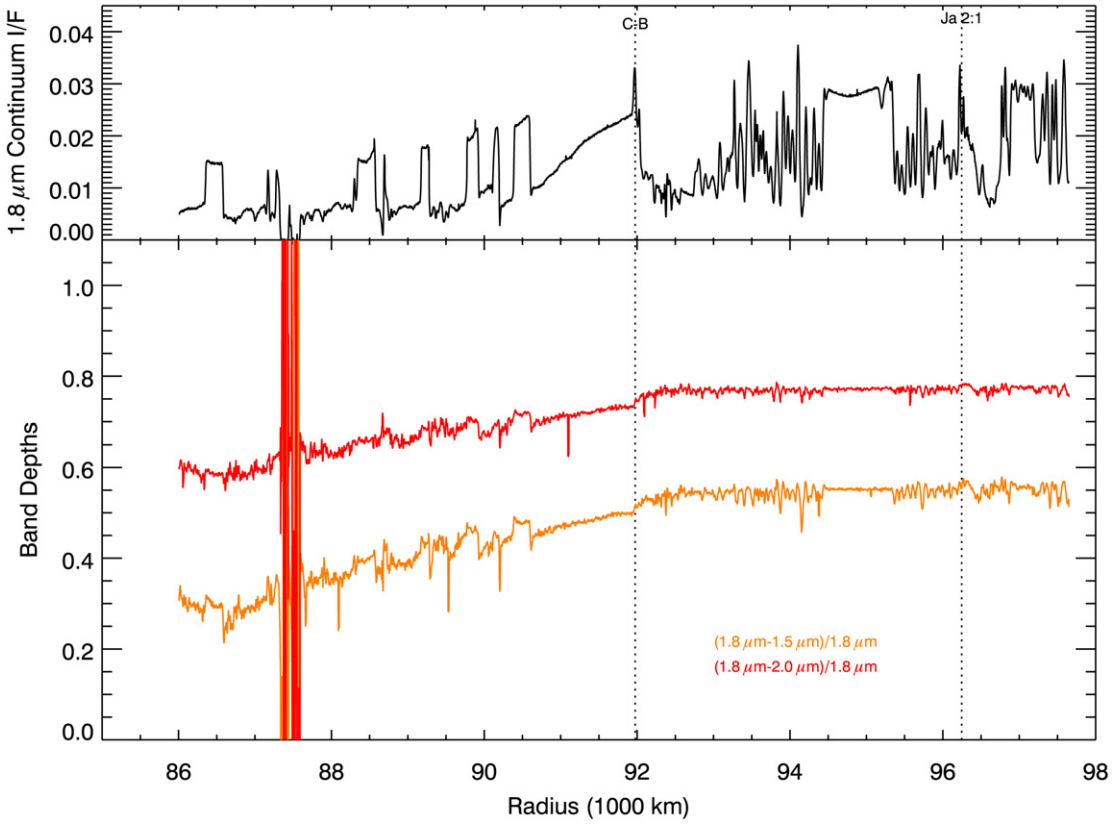

Fig. 26. Band depths, D_B, from SOI scan 1 across the outer C and inner B rings. The lower panel shows the depths of the strong 1.5 and 2.0 μm ice bands derived from the VIMS-IR data. The band depths have been smoothed over 5 radial samples. The top panel shows the I/F profile at the continuum wavelength of 1.8 μm for context. Vertical dotted lines indicate the locations of selected satellite resonances, as labelled, as well as major ring boundaries as listed by French et al. (1993). The noisy region at 87,500 km corresponds to the Maxwell Gap.

7.2. Cassini Division and the A ring (scan 2)

Fig. 27 shows the IR spectra of the Cassini Division, its outer 'ramp,' and five subregions within the A ring. The latter include the two relatively narrow but spectrally quite distinct zones between the Encke and Keeler Gaps and outside the Keeler Gap. The Cassini Division and its outer ramp show weak water ice bands at 1.5 and 2.0 μm, and a distinctive red continuum slope between 0.85 and 1.4 μm. This slope is very different from the blue slope characteristic of clean water ice in this region—as exhibited by all five A ring spectra in the same figure—and may be related to the putative 'silicate' feature seen in the C ring and its ramp. Across the A ring we see much stronger ice bands at 1.5 and 2.0 μm relative to the Cassini Division, while the intrinsically-weaker overtone bands at 1.04 and 1.28 μm also become more prominent. Note the appearance of the 3.10 μm Fresnel peak in all A ring regions, and the unusually strong 3.6 μm peak in the trans-Keeler region, suggestive of very small regolith ice grain sizes (∼10 μm).

The visible spectra of this region are also very similar, with low reflectivities in the blue and much higher reflectivities in the red. The substantial uniformity of the overall spectral behavior as well as the absence of characteristic spectral signatures in the visible led us to investigate the spatial variability of the spectral slopes, evaluated from linear fits to the regions shortward and longward of the pronounced inflection at ∼0.55 μm (see Fig. 3). The blue slope corresponds to the range 0.35–0.55 μm, while the red slope corresponds to 0.55–1.05 μm. The spectra were first normalized at 0.55 μm to remove radial brightness variations; we choose this wavelength to divide the two spectral ranges as the intersection of the two linear fits usually falls near this position.

To facilitate comparisons between the IR and VIS data, we convert the slopes into spectral ratios analogous to the water–ice band depths. From the blue slope we compute the quantity:

$$R_b = \frac{I/F_{0.55} - I/F_{0.35}}{I/F_{0.55}} \tag{9}$$

and for the red slope we compute

$$R_r = \frac{I/F_{1.05} - I/F_{0.55}}{I/F_{0.55}}. \tag{10}$$

Note that these ratios are larger when the slopes are steeper (i.e., redder).

Fig. 28 illustrates the observed trends in the visual spectral slopes and water–ice absorption bands throughout scan 2. Here we first observe an abrupt weakening of the ice bands across the Huygens Gap, as we move from the outermost part of the B-ring to the inner part of the Cassini Division. The band depths are then fairly constant across the Cassini Division, until they begin to strengthen rapidly across the triple feature at 120,700 km and then more slowly across the outer ramp and on into the inner

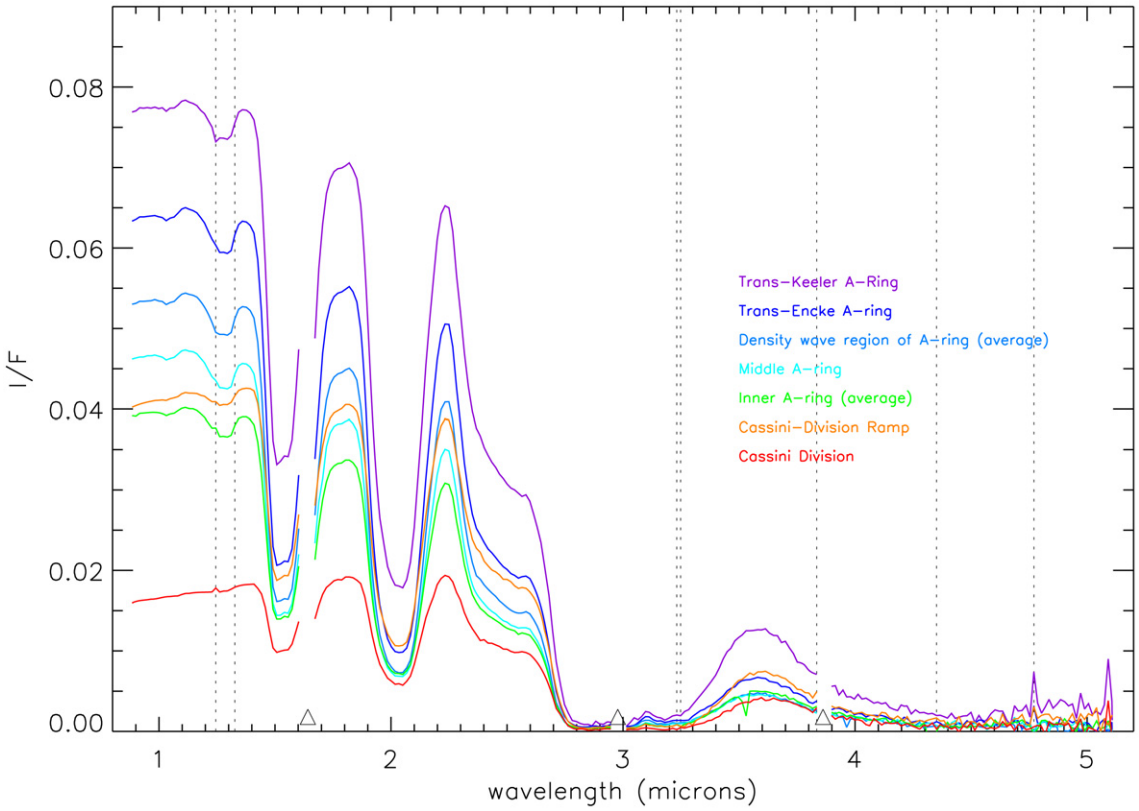

Fig. 27. Infrared spectra of the Cassini Division, its outer ramp, and five regions within the A ring derived from the second VIMS SOI scan. Triangles indicate gaps between the IR focal plane blocking filters where the spectra may be unreliable; these channels have been suppressed. Vertical dotted lines indicate hot pixels, which can saturate in long integrations. Trans-Encke refers to the region between the Encke and Keeler Gaps, while trans-Keeler refers to the region outside the Keeler Gap. The boundary between the density wave region and the middle A-ring is at 129,500 km, and the boundary between the middle and inner A-ring is at 126,000 km.

A ring. This mirrors the transition between the C ring and the B ring described above. In this case, however, the band depths do not quickly stabilize in the inner part of the A ring. Instead, there is a series of transitions which are apparently related to the irregular I/F structure in this part of the ring. Within the Cassini Division itself there is very little, if any, small-scale correlation between optical depth and ice band strength, again implying negligible inter-particle scattering as we found in the C ring.

The band-depths in the A ring finally stabilize near 124,500 km, just interior to the strong Janus 4:3 density wave. Outside this radius, the ice band depths continue to strengthen gradually as far as the Encke Gap, beyond which they begin to weaken slowly. About 500 km interior to the Keeler Gap this trend accelerates rapidly, and beyond the Keeler Gap the ice bands are weaker than at any other location in the A ring. These variations suggest that regolith ice grain sizes are systematically smaller in the innermost and outermost parts of the A ring than they are in the central A ring. (An alternative explanation would be to invoke a minimum in contamination by non-icy material in the central A ring, but there is no other spectral evidence for this hypothesis.)

Most smaller-scale variations in band depth within the A ring are associated with the ubiquitous density waves in this part of the rings. Each of the three strong Janus waves (4:3, 5:4 and 6:5) as well as the Mimas 5:3 density wave shows a decrease in continuum I/F and an increase in ice-band depth coincident with the observed wavetrain. However, these resonances also show a slight *decrease* in the band depths over a region which extends ∼500 km on either side of the wave and coincides spatially with the bright "halos" seen in the I/F profile of the A ring (cf. Fig. 18 above). Apparently the strong density waves have a regional-scale impact on the particle properties in the rings which extends well beyond the actual wavetrains. (Density waves such as these which are driven at Inner Lindblad resonances propagate outwards from the resonance location, whereas the halos are seen on both sides of the resonances.) Perhaps small grains ejected by collisions from ring particles in the wave itself are being transported radially and redeposited throughout the halo regions. Enhanced collision rates (or velocities) within the strong wave regions may compact the surfaces of the ring particles so that their ejecta yields and speeds are larger than those of normal "fluffy" ring particles elsewhere. Another possibility is that an enhanced collisional regime within strong density waves results in the surface layers of the ring particles, which are contaminated by meteoritic debris, being stripped off and redistributed ballistically into the halos, while the cleaner ice cores remain within the wave regions themselves (L.W. Esposito, private communication).

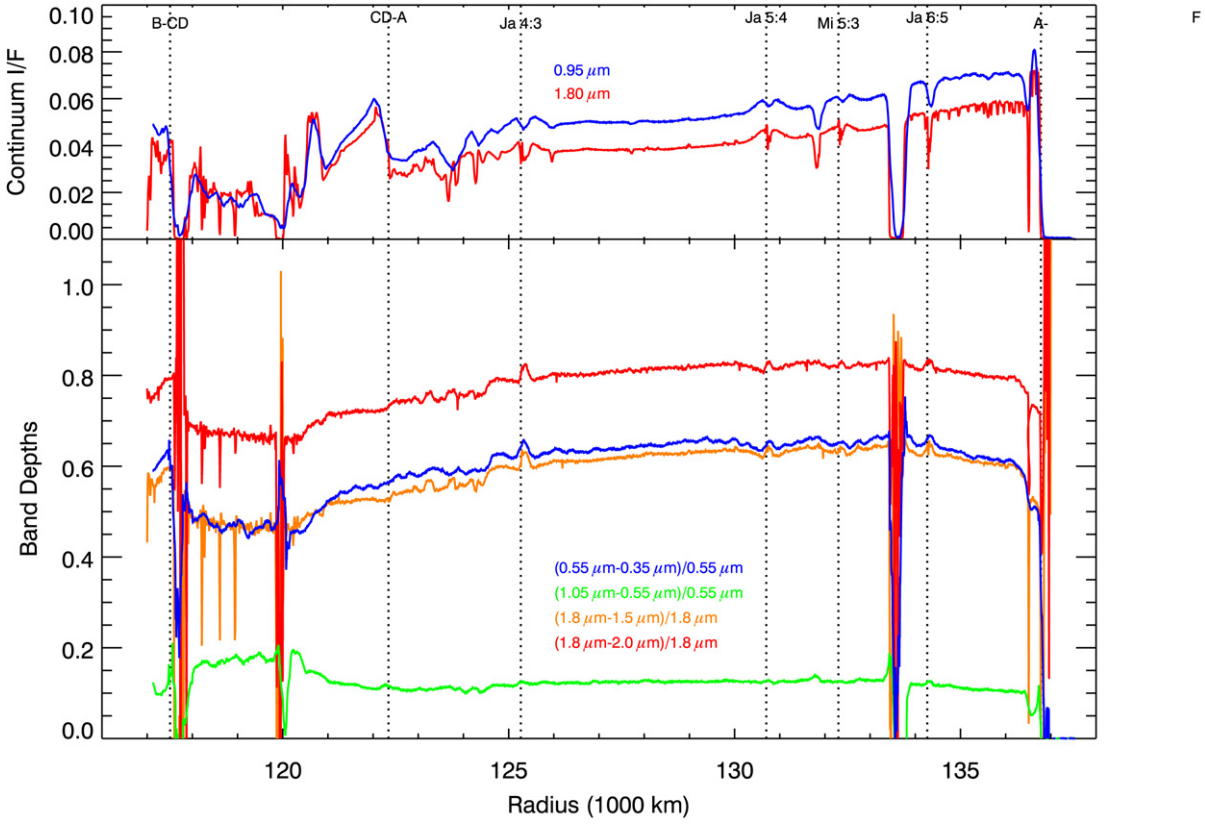

Fig. 28. Band depths, D_B, and spectral slopes from SOI scan 2 across the Cassini Division and A ring. The lower panel shows the depths of the strong 1.5 and 2.0 μm ice bands derived from the VIMS-IR data, as well as the quantities R_b and R_r derived from the spectral slopes between 0.35 and 0.55 μm and between 0.55 and 1.05 μm in the VIMS-V data. The top panel shows the I/F profile at the continuum wavelengths of 0.95 μm from the VIS channel and 1.8 μm from the IR channel for context. Vertical dotted lines indicate the locations of selected satellite resonances, as labelled, as well as major ring boundaries as listed by French et al. (1993). Note the characteristic variations in color and band depth around each of the strong Janus density waves. The noisy regions at 117,800, 120,000, 133,500 km correspond to gaps in the rings.

Note that the Mimas 5:3 bending wave, which appears as a prominent dip in the I/F profile at 131,800 km, shows no clear signature in the band depth profiles. As noted above, because they involve out-of-plane rather than radial perturbations to ring particle orbits, bending waves are less likely than density waves to lead to higher collision rates.

Turning our attention to the visual spectral ratios, the most striking feature that emerges is the tight correlation between the radial variations in the blue slope and the water–ice band strengths. The shifts in the blue slope (the blue curve in Fig. 28) at the outer edge of the B ring, the Cassini Division ramp, and the Keeler Gap all mirror changes in the near-IR water–ice band strengths (denoted by the orange and red curves). Even the transition at 124,500 km and the signatures associated with the strong density waves also appear in the blue slopes. For the blue visual slope to track the water–ice band strength so well, the effective optical path-length through the coloring agent responsible for the blue slope must scale with the effective optical path length through the water ice. This coloring agent therefore appears to be molecularly (or intra-) mixed with the ice throughout the A ring and Cassini Division, consistent with the conclusions of Cuzzi and Estrada (1998) and Poulet et al. (2003). (Recall the discussion in Section 5.1.2 above.)

By contrast, the radial variations in the red slope (the green curve in Fig. 28) do not follow the trends observed in the ice bands or the blue slope. The red slope is found to be steeper in the Cassini Division, lower in the A ring, and lowest in the trans-Keeler region. The coloring agent responsible for the red slope therefore cannot be uniformly intra-mixed with the ice throughout the rings. Instead, there seems to be fractionally more of this material in the Cassini Division than the A ring. This is consistent with a contaminant introduced into the rings by cometary bombardment. As proposed by Cuzzi and Estrada (1998), such a contaminant would have a more pronounced effect on low-optical depth regions like the Cassini Division than on optical thicker regions like the A ring. The red slope may therefore be characteristic of the material responsible for darkening the Cassini division, and presumably also the C ring.

7.3. Comparisons between the two scans

An alternative way of looking at the variations in ice band strength across the rings is presented in Fig. 29, in the form of a scatter plot of the (normalized) 3.6 μm reflectance peak (the mean normalized I/F between 3.4 and 3.8 μm) vs the (normalized) reflectance in the 1.5 μm ice band. To first order, we see

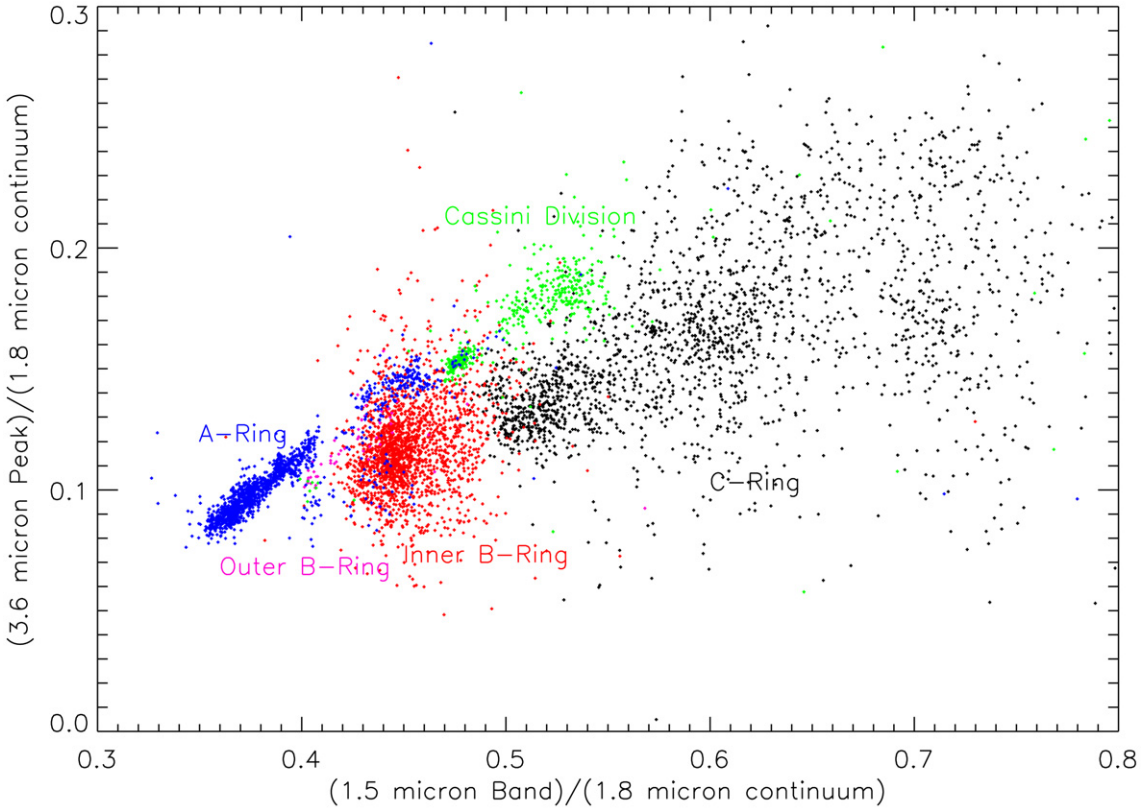

Fig. 29. Scatter plot of the 3.6 μm peak I/F vs the I/F in the bottom of the 1.5 μm ice band, both normalized to the continuum I/F at 1.8 μm. Different colors indicate data from the four major ring regions, with a distinction being made between the inner B ring as seen in scan 1 and the outermost B ring as seen in scan 2. While the ice bands are weakest in the C ring and Cassini Division, these two regions clearly do not have identical spectra, as was seen in Fig. 3 above. However, this plot suggests the existence of two "ring-complexes," with a possible continuous evolutionary trend from the C ring to the B ring, and another from the Cassini Division to the A ring.

that the height of the 3.6 μm peak is positively correlated with the reflectance in the 1.5 μm band. (That is, a weaker 1.5 μm absorption—implying a higher 1.5/1.8 μm ratio—is associated with a higher maximum at 3.6 μm due to weaker ice absorptions at 2.9 and 4.5 μm.)

However, this plot also highlights subtle differences in the spectra from the two scans. The A ring and Cassini Division all fall along a single well-defined "track" extending from the lower left to the upper right of the plot. This trend reflects the continuous changes in water–ice band depths across the A ring and into the Cassini Division seen in Fig. 28. The data from the B and C rings fall along a similar, roughly parallel track, although the scatter about the main trend is larger here owing to the lower signal-to-noise in these data. (Note in Figs. 5 and 6 that while the average I/F in the C ring and inner B ring is 0.005–0.02, that in the A ring and Cassini Division is 0.02–0.05.) The tracks followed by the A ring/Cassini Division and the B/C rings, however, are not identical. Although it might be suspected that this dichotomy is due in some way to the differing viewing geometries of the two SOI scans (cf. Table 1), it has been confirmed in subsequent VIMS radial scans of the entire ring system made under uniform viewing conditions, in both reflected and diffusely-transmitted light, verifying that there is indeed a subtle but pervasive difference between the spectra of these two major ring regions.

The combination of the continuous trend within each track and the clear distinction between the tracks suggests that Saturn's main rings might usefully be thought of as consisting of two "ring-complexes," each composed of an optically thick outer region (the A or B ring), and an optically thin inner region (the Cassini Division or C ring). These two systems show similar large-scale trends in composition, particle size distribution and optical depth, which may provide clues as to how the rings are formed and maintained. The parallels in the structure of the transitions between the optical thick and optically thin regions of these complexes have already been studied in the context of ballistic transport models (Durisen et al., 1989, 1992). Similar analyses of the large-scale spectral gradients seen in the VIMS SOI data may eventually provide further insights into the radial redistribution of material within the rings. The pervasive but subtle differences in the infrared spectra of these two ring complexes may also reflect distinctive features in their dynamics or evolutionary histories.

8. Conclusions

We summarize here our principal results, referring to the relevant figure(s), and end with some suggestions for future work.

(1) VIMS data obtained at SOI cover the outer C and inner B rings (IR only), the Cassini Division and entire A ring, at a

radial resolution in the 1–5 μm range which varies from 15 to 30 km (Fig. 2).

(2) The spectra of all the major regions sampled are dominated by water ice, with typical regolith grain radii of 5–20 μm (Figs. 3 and 4). The presence of relatively weak overtone bands at 1.04 and 1.28 μm indicates that the surfaces of particles in the A ring, where the ice bands are strongest, must be composed of almost pure water ice. The weakest ice bands are found in the C ring and Cassini Division, suggesting smaller grain sizes and/or a greater abundance of a non-icy absorber in these regions.

(3) No specific evidence is found for other ices or CH-bearing organic material in the VIMS SOI spectra, but a broad, shallow absorption feature centered near 1.2 μm—most prominent in the C ring and Cassini Division—may be consistent with Fe^{2+} in silicate minerals (Figs. 3, 25 and 27). A solid identification of this feature, however, will require additional data at a range of phase angles.

(4) The middle C ring data show spectral features characteristic of simple organic molecules (Figs. 7 and 25), but these are almost certainly due to contamination from the planet, as light reaching this part of the rings passed through the upper levels of Saturn's atmosphere.

(5) When displayed in a 2D format, the VIMS SOI data reveal a familiar pattern of radial brightness variations due to the rings' underlying optical depth profile, as well as more subtle spectral variations on both regional and local scales (Figs. 7 and 8). In particular, the strength of the water ice bands changes quite gradually across the boundaries between the C and B rings and between the Cassini Division and A ring, perhaps reflecting the influence of ballistic transport processes in sculpting these regions (Durisen et al., 1992).

(6) The observed radial variations in reflectance (I/F) across the two SOI scans are strongly correlated with optical depth and closely match the structure seen in Voyager imaging profiles obtained under comparable viewing conditions (Figs. 11–19). In particular, structure in the lower-optical-depth C ring and Cassini Division is seen in "normal" contrast, similar to the Voyager 2 reflected-light profile (Figs. 11, 12 and 15), while structure in the more opaque B and inner A rings is seen in "reverse" contrast, similar to the Voyager 1 transmitted-light profile (Figs. 13, 14, and 16–19).

(7) Of particular note is the quasi-periodic structure which dominates the inner B ring, and which appears to be unchanged in amplitude and phase over an interval of 24 years (Figs. 13 and 14).

(8) A simple analytic model of light transmission through a vertically-extended slab, neglecting interparticle scattering, provides excellent fits to the observed I/F profiles in the C ring and Cassini Division and an acceptable fit to the inner B ring (Figs. 20–22). This model is less successful in the A ring, where a steady increase in I/F with radius suggests either a slowly-varying particle phase function or a vertically-thinner ring (Figs. 23 and 24). As noted in previous photometric studies of the A ring (e.g., Dones et al., 1993), the regions exterior to the Encke and Keeler Gaps are particularly anomalous.

An additional complication is the azimuthally-variable average optical depth associated with "self-gravity wakes" in the A ring, which makes the 'correct' choice of optical depth profile somewhat problematic. Potentially even more serious for simple photometric models such as that employed here is the fact that, in reality, the middle A ring appears to be a mixture of almost opaque wakes and relatively transparent interwake zones (Colwell et al., 2006; Hedman et al., 2007).

(9) Water ice band depths vary systematically across the rings, gradually becoming stronger as we move from the C ring into the B ring or from the Cassini Division into the A ring, as illustrated in Figs. 26 and 28. These variations probably reflect variations in regolith grain size and/or ice purity, in the sense that the ice grains in the A and B rings are larger and/or more pure than those in the C ring and Cassini Division.

(10) An extremely tight correlation between the IR ice band strengths and the slope of the visible spectrum shortward of 0.55 μm across the Cassini Division and A ring strongly suggests that the non-icy component (possibly tholins) responsible for this "blue slope" is mixed within the ice grains at the molecular level (Fig. 28).

(11) No such correlation is observed for the visible slope longward of 0.55 μm, variations in which may instead trace the more neutral-colored material responsible for the visible darkening of the C ring and Cassini Division (Cuzzi and Estrada, 1998).

(12) The band depths in the C ring plateaux are only slightly stronger than the band depths in the background C ring, despite the strong optical depth contrast between these regions (Fig. 26). This indicates that interparticle scattering is relatively unimportant in the SOI geometry. A similar lack of correlation is seen in the Cassini Division (Fig. 28). Subtle variations in the band depths in the inner B ring are correlated with the quasi-periodic variations in optical depth and I/F across this region, but the correlation is in the opposite sense to that expected for interparticle scattering.

(13) The strong density waves in the A ring are generally characterized by a lower I/F and stronger ice bands but are surrounded by regions of enhanced I/F and reduced band strength 1000–1400 km wide (Figs. 24 and 28). These "halos" suggest that the density waves are influencing the effective grain size and/or ice purity of ring particle regoliths over an extended region. The nearby strong Mimas 5:3 bending wave does not generate a similar halo.

(14) The trans-Keeler region of the A ring is anomalously bright (Fig. 24), indicating a higher single-particle albedo and/or a flatter phase function than the rest of the A ring (Dones et al., 1993). This region also exhibits very weak ice bands, implying a change in the nature of the ring particle regoliths (Fig. 28).

(15) There is a subtle but pervasive difference in the spectra between the B/C rings and the A ring/Cassini Division, illustrated in Fig. 29, which suggests that these two "ring complexes" may have somewhat different compositions and histories.

Future progress in quantitatively interpreting the VIMS spectra presented in this paper will depend on the development of a radiative transfer model for the rings which can properly

handle rings with high packing densities as well as the diffuse transmission geometry at SOI. A useful intermediate step, along similar lines to the study by Poulet et al. (2003), would be to model the rings as an ensemble of mini-satellites, neglecting interparticle scattering completely, with the goal of deriving average regolith grain sizes and the fractional abundance of non-icy contaminants (e.g., tholins and/or meteoritic material).

In closing, we note that the spectral data presented in this paper, while unlikely to be surpassed in spatial resolution in the foreseeable future, represent only the first installment on what is expected to be an extensive archive of VIS-IR spectral data for Saturn's rings covering a wide range of illumination and viewing geometries. These include observations, many already in hand, at near-zero and very high phase angles as well as many intermediate values; at large and small emission angles; and on both sunlit and dark sides of the rings.

Acknowledgments

We thank the VIMS engineering and operational teams, without whom neither the instrument nor any of the data presented here would exist. We also acknowledge the work of Brad Wallis and the SOI target working team, whose lengthy deliberations led to a workable compromise for the design of this unique opportunity in the Cassini orbital tour. Thanks are also due to Ron Draper, Cassini's first project manager, whose early encouragement in the face of engineering skepticism led to the first investigations of the unique science which could be done at SOI; to later managers Bob Mitchell and Earl Maize for their unstinting support before several critical review boards; and to the dedicated mission planners, navigators and engineers at JPL who made it all actually work. This work was carried out with support from NASA and the Cassini–Huygens Project, under Contract 961171.

References

Bergren, M.S., Schuh, D., Sceats, M.G., Rice, S.A., 1978. The OH stretching region infrared spectra of low density amorphous solid water and polycrystalline ice Ih. J. Chem. Phys. 69, 3477–3482.

Borderies, N., Goldreich, P., Tremaine, S., 1985. A granular flow model for dense planetary rings. Icarus 63, 406–420.

Brown, R.H., and 21 colleagues, 2004. The Cassini Visual and Infrared Mapping Spectrometer (VIMS) investigation. Space Sci. Rev. 115, 111–168.

Brown, R.H., and 25 colleagues, 2006. Observations in the Saturn system during approach and orbital insertion, with Cassini's Visual and Infrared Mapping Spectrometer (VIMS). Astron. Astrophys. 446, 707–716.

Chandrasekhar, S., 1960. Radiative Transfer. Dover, New York.

Clapp, M.L., Miller, R.E., Worsnop, D.R., 1995. Frequency dependent optical constants of water ice obtained directly from aerosol extinction spectra. J. Phys. Chem. 99, 6317–6326.

Clark, R.N., 1980. Ganymede, Europa, Callisto, and Saturn's rings—Compositional analysis from reflectance spectroscopy. Icarus 44, 388–409.

Clark, R.N., 1981a. The spectral reflectance of water–mineral mixtures at low temperatures. J. Geophys. Res. 86, 3074–3086.

Clark, R.N., 1981b. Water frost and ice—The near-infrared spectral reflectance 0.65–2.5 microns. J. Geophys. Res. 86, 3087–3096.

Clark, R.N., 1982. Implications of using broadband photometry for compositional remote sensing of icy objects. Icarus 49, 244–257.

Clark, R.N., 1999. Spectroscopy of rocks and minerals and principles of spectroscopy. In: Rencz, A.N. (Ed.), Manual of Remote Sensing. John Wiley and Sons, New York, pp. 3–58. Chap. 1.

Clark, R.N., Lucey, P.G., 1984. Spectral properties of ice–particulate mixtures and implications for remote sensing. I. Intimate mixtures. J. Geophys. Res. 89, 6341–6348.

Clark, R.N., McCord, T.B., 1980. The rings of Saturn—New near-infrared reflectance measurements and a 0.326–4.08 micron summary. Icarus 43, 161–168.

Clark, R.N., Roush, T.L., 1984. Reflectance spectroscopy—Quantitative analysis techniques for remote sensing applications. J. Geophys. Res. 89, 6329–6340.

Clark, R.N., Fanale, F.P., Gaffey, M.J., 1986. Surface composition of natural satellites. In: Burns, J.A., Matthews, M.S. (Eds.), Satellites. IAU Colloq. 77. University of Arizona Press, Tucson, pp. 437–491.

Clark, R.N., Swayze, G.A., Wise, R., Livo, E., Hoefen, T., Kokaly, R., Sutley, S.J., 2003. USGS Digital Spectral Library splib05a, U.S. Geological Survey Open-File Report 03-395. http://pubs.usgs.gov/of/2003/ofr-03-395.

Clark, R.N., and 25 colleagues, 2005a. Compositional maps of Saturn's moon Phoebe from imaging spectroscopy. Nature 435, 66–69.

Clark, R.N., and 24 colleagues, 2005b. Cassini VIMS compositional mapping of surfaces in the Saturn system and the role of water, cyanide compounds and carbon dioxide. Bull. Am. Astron. Soc. 37, 705.

Clark, R.N., and 24 colleagues, 2005c. Compositional mapping of surfaces in the Saturn system with Cassini VIMS: The role of water, cyanide compounds and carbon dioxide. AGU Fall Meeting Abstracts P22-A2.

Clark, R.N., and 11 colleagues, 2007. Compositional mapping of Saturn's satellite Dione with Cassini VIMS and implications for dark material in the Saturn system. Icarus, doi:10.1016/j.icarus.2007.08.035, in press.

Colombo, G., Goldreich, P., Harris, A.W., 1976. Spiral structure as an explanation for the asymmetric brightness of Saturn's A ring. Nature 264, 344–345.

Colwell, J.E., Esposito, L.W., Sremčević, M., 2006. Self-gravity wakes in Saturn's A ring measured by stellar occultations from Cassini. Geophys. Res. Lett. 33. 7201.

Cooke, M.L., 1991. Saturn's rings: Photometric studies of the C ring and radial variation in the Keeler Gap. Ph.D. thesis, Cornell University.

Coradini, A., Filacchione, G., Capaccioni, F., Cerroni, P., Adriani, A., Brown, R.H., Langevin, Y., Gondet, B., 2004. Cassini/VIMS-V at Jupiter: Radiometric calibration test and data results. Planet. Space Sci. 52, 661–670.

Cruikshank, D.P., and 14 colleagues, 1998. The composition of Centaur 5145 Pholus. Icarus 135, 389–407.

Cruikshank, D.P., Imanaka, H., Dalle Ore, C.M., 2005a. Tholins as coloring agents on outer Solar System bodies. Adv. Space Res. 36, 178–183.

Cruikshank, D.P., Owen, T.C., Dalle Ore, C.M., Geballe, T.R., Roush, T.L., de Bergh, C., Sandford, S.A., Poulet, F., Benedix, G.K., Emery, J.P., 2005b. A spectroscopic study of the surfaces of Saturn's large satellites: H_2O ice, tholins, and minor constituents. Icarus 175, 268–283.

Cuzzi, J.N., Estrada, P.R., 1998. Compositional evolution of Saturn's rings due to meteoroid bombardment. Icarus 132, 1–35.

Cuzzi, J.N., Pollack, J.B., 1978. Saturn's rings: Particle composition and size distribution as constrained by microwave observations. I. Radar observations. Icarus 33, 233–262.

Cuzzi, J.N., Pollack, J.B., Summers, A.L., 1980. Saturn's rings: Particle composition and size distribution as constrained by observations at microwave wavelengths. II. Radio interferometric observations. Icarus 44, 683–705.

Cuzzi, J.N., Lissauer, J.J., Esposito, L.W., Holberg, J.B., Marouf, E.A., Tyler, G.L., Boischot, A., 1984. Saturn's rings: Properties and processes. In: Greenberg, R., Brahic, A. (Eds.), Planetary Rings. University of Arizona Press, Tucson, pp. 73–199.

Cuzzi, J.N., French, R.G., Dones, L., 2002. HST multicolor (255–1042 nm) photometry of Saturn's main rings I: Radial profiles, phase and opening angle variations, and regional spectra. Icarus 158, 199–223.

Dones, L., Cuzzi, J.N., Showalter, M.R., 1993. Voyager photometry of Saturn's A ring. Icarus 105, 184–215.

Doyle, L.R., Dones, L., Cuzzi, J.N., 1989. Radiative transfer modeling of Saturn's outer B ring. Icarus 80, 104–135.

Durisen, R.H., 1995. An instability in planetary rings due to ballistic transport. Icarus 115, 66–85.

Durisen, R.H., Cramer, N.L., Murphy, B.W., Cuzzi, J.N., Mullikin, T.L., Cederbloom, S.E., 1989. Ballistic transport in planetary ring systems due to particle erosion mechanisms. I. Theory, numerical methods, and illustrative examples. Icarus 80, 136–166.

Durisen, R.H., Bode, P.W., Cuzzi, J.N., Cederbloom, S.E., Murphy, B.W., 1992. Ballistic transport in planetary ring systems due to particle erosion mechanisms. II. Theoretical models for Saturn's A- and B-ring inner edges. Icarus 100, 364–393.

Epstein, E.E., Janssen, M.A., Cuzzi, J.N., 1984. Saturn's rings—3-mm low-inclination observations and derived properties. Icarus 58, 403–411.

Esposito, L.W., O'Callaghan, M., Simmons, K.E., Hord, C.W., West, R.A., Lane, A.L., Pomphrey, R.B., Coffeen, D.L., Sato, M., 1983a. Voyager photopolarimeter stellar occultation of Saturn's rings. J. Geophys. Res. 88, 8643–8649.

Esposito, L.W., and 10 colleagues, 1983b. Eccentric ringlet in the Maxwell gap at 1.45 Saturn radii: Multi-instrument Voyager observations. Science 222, 57–60.

Esposito, L.W., Cuzzi, J.N., Holberg, J.B., Marouf, E.A., Tyler, G.L., Porco, C.C., 1984. Saturn's rings: Structure, dynamics, and particle properties. In: Gehrels, T., Matthews, M. (Eds.), Saturn. University of Arizona Press, Tucson, pp. 463–545.

Estrada, P.R., Cuzzi, J.N., 1996. Voyager observations of the color of Saturn's rings. Icarus 122, 251–272.

Estrada, P.R., Cuzzi, J.N., Showalter, M.R., 2003. Voyager color photometry of Saturn's main rings: A correction. Icarus 166, 212–222.

Filacchione, G., and 28 colleagues, 2007. Saturn's icy satellites investigated by Cassini-VIMS.I. Full-disk properties: 350–5100 nm reflectance spectra and phase curves. Icarus 186, 259–290.

Flynn, B.C., Cuzzi, J.N., 1989. Regular structure in the inner Cassini Division of Saturn's rings. Icarus 82, 180–199.

French, R.G., Nicholson, P.D., 2000. Saturn's rings II. Particle sizes inferred from stellar occultation data. Icarus 145, 502–523.

French, R.G., and 17 colleagues, 1993. Geometry of the Saturn system from the 3 July 1989 occultation of 28 Sgr and Voyager observations. Icarus 103, 163–214.

French, R., Salo, H., McGhee, C., Dones, L., 2006. Azimuthal brightness asymmetry in Saturn's A and B rings. COSPAR Sci. Assembly 36, 3323.

Goertz, C.K., Morfill, G., 1988. A new instability of Saturn's ring. Icarus 74, 325–330.

Goldstein, R.M., Morris, G.A., 1973. Radar observations of the rings of Saturn. Icarus 20, 260–262.

Goldstein, R.M., Green, R.R., Pettengill, G.H., Campbell, D.B., 1977. The rings of Saturn—Two-frequency radar observations. Icarus 30, 104–110.

Gradie, J., Thomas, P., Veverka, J., 1980. The surface composition of Amalthea. Icarus 44, 373–387.

Grossman, A.W., 1990. Microwave imaging of Saturn's deep atmosphere and rings. Ph.D. thesis, California Institute of Technology.

Grundy, W.M., Schmitt, B., 1998. The temperature-dependent near-infrared absorption spectrum of hexagonal H_2O ice. J. Geophys. Res. 103, 25809–25822.

Hansen, G.B., McCord, T.B., 2004. Amorphous and crystalline ice on the Galilean satellites: A balance between thermal and radiolytic processes. J. Geophys. Res. Planets 109. E01012.

Hansen, G., and 23 colleagues, 2005. Ice grain size distribution: Differences between jovian and saturnian icy satellites from Galileo and Cassini measurements. Bull. Am. Astron. Soc. 37, 729.

Hedman, M.M., Nicholson, P.D., Salo, H., Wallis, B.D., Buratti, B.J., Baines, K.H., Brown, R.H., Clark, R.N., 2007. Self-gravity wake structures in Saturn's A ring revealed by Cassini VIMS. Astron. J. 133, 2624–2629.

Holberg, J.B., Forrester, W.T., Lissauer, J.J., 1982. Identification of resonance features within the rings of Saturn. Nature 297, 115–120.

Horn, L.J., Cuzzi, J.N., 1996. Characteristic wavelengths of irregular structure in Saturn's B ring. Icarus 119, 285–310.

Irvine, W.M., Lane, A.P., 1973. Photometric properties of Saturn's rings. Icarus 18, 171–176.

Karkoschka, E., 1994. Spectrophotometry of the jovian planets and Titan at 300- to 1000-nm wavelength: The methane spectrum. Icarus 111, 174–192.

Kuiper, G.P., 1952. Planetary atmospheres and their origin. In: Kuiper, G.P. (Ed.), The Atmospheres of the Earth and Planets. University of Chicago Press, Chicago, pp. 306–405.

Kuiper, G.P., 1957. Infrared observations of planets and satellites. Astron. J. 62, 245 (abstract).

Kuiper, G.P., Cruikshank, D.P., Fink, U., 1970. The composition of Saturn's rings. Sky Telescope 39 (2), 14–80 (letter to editor).

Lane, A.L., Hord, C.W., West, R.A., Esposito, L.W., Coffeen, D.L., Sato, M., Simmons, K.E., Pomphrey, R.B., Morris, R.B., 1982. Photopolarimetry from Voyager 2—Preliminary results on Saturn, Titan, and the rings. Science 215, 537–543.

Lebofsky, L.A., Fegley Jr., M.B., 1976. Laboratory reflection spectra for the determination of chemical composition of ice bodies. Icarus 28, 379–387.

Lebofsky, L.A., Johnson, T.V., McCord, T.B., 1970. Saturn's rings: Spectral reflectivity and compositional implications. Icarus 13, 226–230.

Lin, D.N.C., Bodenheimer, P., 1981. On the stability of Saturn's rings. Astrophys. J. 248, L83–L86.

Lissauer, J.J., Cuzzi, J.N., 1982. Resonances in Saturn's rings. Astron. J. 87, 1051–1058.

Lukkari, J., 1981. Collisional amplification of density fluctuations in Saturn's rings. Nature 292, 433–435.

Marouf, E.A., Tyler, G.L., Zebker, H.A., Simpson, R.A., Eshleman, V.R., 1983. Particle size distributions in Saturn's rings from Voyager 1 radio occultation. Icarus 54, 189–211.

Marouf, E.A., Tyler, G.L., Rosen, P.A., 1986. Profiling Saturn's rings by radio occultation. Icarus 68, 120–166.

McCord, T.B., and 24 colleagues, 2004. Cassini VIMS observations of the Galilean satellites including the VIMS calibration procedure. Icarus 172, 104–126.

Moroz, V.I., 1967. Physika Planet. Nauka, Moscow (in Russian).

Nicholson, P.D., Cooke, M.L., Pelton, E., 1990. An absolute radius scale for Saturn's rings. Astron. J. 100, 1339–1362.

Nicholson, P.D., French, R.G., Tollestrup, E., Cuzzi, J.N., Harrington, J., Matthews, K., Perkovic, O., Stover, R.J., 2000. Saturn's rings. I. Optical depth profiles from the 28 Sgr occultation. Icarus 145, 474–501.

Nicholson, P.D., French, R.G., Campbell, D.B., Margot, J.-L., Nolan, M.C., Black, G.J., Salo, H.J., 2005. Radar imaging of Saturn's rings. Icarus 177, 32–62.

Ostro, S.J., Pettengill, G.H., Campbell, D.B., 1980. Radar observations of Saturn's rings at intermediate tilt angles. Icarus 41, 381–388.

Pettengill, G.H., Hagfors, T., 1974. Comment on radar scattering from Saturn's rings. Icarus 21, 188–190.

Pilcher, C.B., Chapman, C.R., Lebofsky, L.A., Kieffer, H.H., 1970. Saturn's rings: Identification of water frost. Science 167, 1372–1373.

Pollack, J.B., 1975. The rings of Saturn. Space Sci. Rev. 18, 3–97.

Pollack, J.B., Summers, A., Baldwin, B., 1973. Estimates of the sizes of the particles in the rings of Saturn and their cosmogonic implications. Icarus 20, 263–278.

Porco, C.C., Nicholson, P.D., 1987. Eccentric features in Saturn's outer C ring. Icarus 72, 437–467.

Porco, C., Nicholson, P.D., Borderies, N., Danielson, G.E., Goldreich, P., Holberg, J.B., Lane, A.L., 1984a. The eccentric saturnian ringlets at 1.29 R_S and 1.45 R_S. Icarus 60, 1–16.

Porco, C., Danielson, G.E., Goldreich, P., Holberg, J.B., Lane, A.L., 1984b. Saturn's nonaxisymmetric ring edges at 1.95 R_S and 2.27 R_S. Icarus 60, 17–28.

Porco, C.C., and 34 colleagues, 2005. Cassini imaging science: Initial results on Saturn's rings and small satellites. Science 307, 1226–1236.

Poulet, F., Cuzzi, J.N., 2002. The composition of Saturn's rings. Icarus 160, 350–358.

Poulet, F., Cruikshank, D.P., Cuzzi, J.N., Roush, T.L., French, R.G., 2003. Compositions of Saturn's rings A, B, and C from high resolution near-infrared spectroscopic observations. Astron. Astrophys. 412, 305–316.

Puetter, R.C., Russell, R.W., 1977. The 2–4-micron spectrum of Saturn's rings. Icarus 32, 37–40.

Salo, H., 1995. Simulations of dense planetary rings. III. Self-gravitating identical particles. Icarus 117, 287–312.

Salo, H., Karjalainen, R., 2003. Photometric modeling of Saturn's rings. I. Monte Carlo method and the effect of nonzero volume filling factor. Icarus 164, 428–460.

Salo, H., Karjalainen, R., French, R.G., 2004. Photometric modeling of Saturn's rings. II. Azimuthal asymmetry in reflected and transmitted light. Icarus 170, 70–90.

Schmit, U., Tscharnuter, W.M., 1999. On the formation of the fine-scale structure in Saturn's B ring. Icarus 138, 173–187.

Shkuratov, Y., Starukhina, L., Hoffmann, H., Arnold, G., 1999. A model of spectral albedo of particulate surfaces: Implications for optical properties of the Moon. Icarus 137, 235–246.

Showalter, M.R., Gordon, M.K., 2004. Voyager 1 and Voyager 2 ISS ring profiles, v 1.0, File VG-2810, NASA Planetary Data System.

Showalter, M.R., Nicholson, P.D., 1990. Saturn's rings through a microscope—Particle size constraints from the Voyager PPS scan. Icarus 87, 285–306.

Showalter, M.R., Bollinger, K.J., Cuzzi, J.N., Nicholson, P.D., 1996. The rings node for the planetary data system. Planet. Space Sci. 44, 33–45.

Smith, B.A., and 26 colleagues, 1981. Encounter with Saturn—Voyager 1 imaging science results. Science 212, 163–191.

Smith, B.A., and 28 colleagues, 1982. A new look at the Saturn system—The Voyager 2 images. Science 215, 504–537.

Thompson, W.T., Lumme, K., Irvine, W.M., Baum, W.A., Esposito, L.W., 1981. Saturn's rings—Azimuthal variations, phase curves, and radial profiles in four colors. Icarus 46, 187–200.

Tiscareno, M.S., Burns, J.A., Hedman, M.M., Porco, C.C., Weiss, J.W., Dones, L., Richardson, D.C., Murray, C.D., 2006a. 100-metre-diameter moonlets in Saturn's A ring from observations of 'propeller' structures. Nature 440, 648–650.

Tiscareno, M.S., Nicholson, P.D., Burns, J.A., Hedman, M.M., Porco, C.C., 2006b. Unravelling temporal variability in Saturn's spiral density waves: Results and predictions. Astrophys. J. 651, L65–L68.

Tokar, R.L., and 12 colleagues, 2005. Cassini observations of the thermal plasma in the vicinity of Saturn's main rings and the F and G rings. Geophys. Res. Lett. 32, 14.

Tremaine, S., 2003. On the origin of irregular structure in Saturn's rings. Astron. J. 125, 894–901.

Turtle, E., Porco, C., Haemmerle, V., Hubbard, W., Clark, R., 1991. The kinematics of eccentric features in Saturn's Cassini Division from combined Voyager and ground-based data. Bull. Am. Astron. Soc. 23, 1179.

Tyler, G.L., Marouf, E.A., Simpson, R.A., Zebker, H.A., Eshleman, V.R., 1983. The microwave opacity of Saturn's rings at wavelengths of 3.6 and 13 cm from Voyager 1 radio occultation. Icarus 54, 160–188.

Ward, W.R., 1981. On the radial structure of Saturn's rings. Geophys. Res. Lett. 8, 641–643.

Wilson, P.D., Sagan, C., Thompson, W.R., 1994. The organic surface of 5145 Pholus: Constraints set by scattering theory. Icarus 107, 288–303.

Young, D.T., and 42 colleagues, 2005. Composition and dynamics of plasma in Saturn's magnetosphere. Science 307, 1262–1266.

Zebker, H.A., Marouf, E.A., Tyler, G.L., 1985. Saturn's rings—Particle size distributions for thin layer models. Icarus 64, 531–548.